



HAL
open science

Novel Hybrid Numerical Simulation of the Wave Equation by Combining Physical and Numerical Representation Theorems and a Review of Hybrid Methodologies

Chao Lyu, Liang Zhao, Yann Capdeville

► **To cite this version:**

Chao Lyu, Liang Zhao, Yann Capdeville. Novel Hybrid Numerical Simulation of the Wave Equation by Combining Physical and Numerical Representation Theorems and a Review of Hybrid Methodologies. *Journal of Geophysical Research: Solid Earth*, 2022, 127 (5), 10.1029/2021JB022368 . hal-03872654

HAL Id: hal-03872654

<https://hal.science/hal-03872654>

Submitted on 25 Nov 2022

HAL is a multi-disciplinary open access archive for the deposit and dissemination of scientific research documents, whether they are published or not. The documents may come from teaching and research institutions in France or abroad, or from public or private research centers.

L'archive ouverte pluridisciplinaire **HAL**, est destinée au dépôt et à la diffusion de documents scientifiques de niveau recherche, publiés ou non, émanant des établissements d'enseignement et de recherche français ou étrangers, des laboratoires publics ou privés.

See discussions, stats, and author profiles for this publication at: <https://www.researchgate.net/publication/360412542>

Novel Hybrid Numerical Simulation of the Wave Equation by Combining Physical and Numerical Representation Theorems and a Review of Hybrid Methodologies

Article in *Journal of Geophysical Research: Solid Earth* · May 2022

DOI: 10.1029/2021JB022368

CITATIONS

3

READS

245

3 authors, including:



Chao Lyu

University of California, Berkeley

9 PUBLICATIONS 66 CITATIONS

[SEE PROFILE](#)



Liang Zhao

Institute of Geology and Geophysics, Chinese Academy of Sciences

125 PUBLICATIONS 2,753 CITATIONS

[SEE PROFILE](#)

Some of the authors of this publication are also working on these related projects:



Seismic observations on subduction zones [View project](#)



Evolution of the Adria-Europe plate boundary [View project](#)

1 **Novel hybrid numerical simulation of the wave equation**
2 **by combining physical and numerical representation**
3 **theorems and a review of hybrid methodologies**

4 **Chao Lyu^{1,2,3}, Liang Zhao¹, Yann Capdeville²**

5 ¹State Key Laboratory of Lithospheric Evolution, Institute of Geology and Geophysics, Chinese Academy
6 of Sciences, 100029 Beijing, China

7 ²Laboratoire de Planétologie et Géodynamique de Nantes, CNRS, Université de Nantes

8 ³University of California, Department of Earth and Planetary Science, Berkeley, CA, USA

9 **Key Points:**

- 10 • Hybrid wave numerical simulation methods of circumventing the heavy compu-
11 tational cost in the global waveform tomography are reviewed.
12 • The proposed hybrid method has the flexible local meshing and is highly accu-
13 rate and memory efficient.
14 • Only three physical quantities located exactly on the hybrid interface are required
15 to construct the hybrid inputs.

Corresponding author: Liang Zhao, zhaoliang@mail.iggcas.ac.cn

This article has been accepted for publication and undergone full peer review but has not been through the copyediting, typesetting, pagination and proofreading process, which may lead to differences between this version and the [Version of Record](#). Please cite this article as doi: [10.1029/2021JB022368](https://doi.org/10.1029/2021JB022368).

This article is protected by copyright. All rights reserved.

Abstract

We present a novel hybrid method to simulate wave propagation through remote regional models. By reviewing and refining the two main existing hybrid categories, the multiple point sources method and direct discrete differentiation method, containing five distinct subcategories, the proposed hybrid method has the following three advantages. (i) The meshing of the local target model is completely independent of that of the global reference model. (ii) Only three physical quantities, i.e., the gradient ∇q , potential q , and second temporal derivative of the potential $\partial_{tt}q$ for the acoustic wave equation (traction, displacement, and acceleration for the elastic scenario) are required to construct the hybrid inputs during the first global simulation. They are located exactly on the two-dimensional (2D) hybrid interface, which is highly accurate and memory efficient for three-dimensional (3D) hybrid numerical simulations. The required memory of hybrid inputs can be reduced fourfold if the very high polynomial degree spectral element method (SEM) is used for the 3D local hybrid simulation. (iii) An efficient artificial perfectly matched layer (PML) can be adopted naturally without any elements overlapping between the local and PML domains in the second hybrid simulation. We build on theoretical analysis and 2D/3D numerical forward simulations based on the SEM to illustrate this new hybrid method and demonstrate its validity. The proposed hybrid method is promising for efficiently probing key 3D structures anywhere within the Earth using the so-called “box tomography.”

1 Plain Language Summary

The seismic structure of the Earth is multi-scale, yet capturing such a broad range of complex heterogeneities using the available global waveform tomography is still computationally prohibitive. It is important to lighten this computational burden by inverting only a small region, namely, the so-called box tomography. As the forward part of box tomography, an efficient implementation of a hybrid numerical simulation is crucial. After reviewing and analyzing the two main existing hybrid methods, including five different subcategories, we propose a new hybrid method, which is highly accurate, memory efficient, and promising for wide use in probing the key 3D structures anywhere within the Earth using the so-called “box tomography.”

2 Introduction

Over the past three decades, with the development of effective computer clusters, efficient numerical methods, such as the finite difference method (FDM) and spectral element method (SEM), improved full waveform inversion (FWI) techniques, and exten-

50 sive global deployment of stations, the imaging of Earth has achieved unprecedented ac-
51 curacy (French & Romanowicz, 2015; Bozdag et al., 2016; Fichtner et al., 2018; Lei et
52 al., 2020). Faster and more accurate calculations of the elastic wavefield within hetero-
53 geneous media are key to developing and improving accurate imaging techniques rely-
54 ing on full-waveform analysis (Tarantola, 1984; Pratt et al., 1998; Virieux & Operto, 2009;
55 Capdeville & Mtivier, 2018; Tromp, 2019; Lyu, Capdeville, Al-Attar, & Zhao, 2021). Earths
56 structure is multi-scale, yet capturing such a broad range of complex heterogeneities with
57 seismic wave propagation across the observable frequency band (e.g., ≥ 1 s) requires thou-
58 sands of global numerical simulations of seismic/acoustic wave equations, which are still
59 computationally prohibitive. Therefore, it is important to lighten this computational bur-
60 den to further increase the resolution and accuracy of imaging. Many research efforts
61 have been devoted to speed up global wave simulations. For example, the real coupling
62 “CSEM” method couples the SEM simulation with normal mode calculations (Capdeville
63 et al., 2003). Another two-step approach is based on the physical domain decomposition,
64 where wave propagation is first performed in the global reference model and the hybrid
65 inputs are calculated and saved only once. Subsequently, they are imposed into the lo-
66 cal target model as the equivalent virtual sources to perform the hybrid simulation (Wen
67 & Helmberger, 1998; Bielak et al., 2003; Chevrot et al., 2004; Chen et al., 2005; L. Zhao
68 et al., 2008; Monteiller et al., 2013; Masson et al., 2014; Tong, Chen, et al., 2014; M. Zhao
69 et al., 2016; Lin et al., 2019; Leng et al., 2020; Pienkowska et al., 2021). Hereafter, we
70 focus on such a two-step approach and refer to it as the “hybrid method” (the hybrid
71 simulation between the global reference and local target models). It can be applied for
72 imaging localized multi-scale heterogeneities in the shallow and deep Earth (Monteiller
73 et al., 2015; Y. Wang et al., 2016; Masson & Romanowicz, 2017a, 2017b; Zhang et al.,
74 2018; Beller et al., 2018; Clouzet et al., 2018; K. Wang, Yang, et al., 2021; K. Wang, Wang,
75 et al., 2021), and it is referred to as the “box tomography” (Masson & Romanowicz, 2017a).
76 Because almost all the forward and backward numerical simulations of wave propaga-
77 tion are confined to the smallest computational volume, local high-frequency numerical
78 simulations can be implemented without difficulty. Moreover, the specially selected spa-
79 tial illumination from remote seismic events and/or stations facilitates higher-resolution
80 imaging. Its principal difficulty results from unknown mediums in the external domain
81 that mask the target structure. Masson and Romanowicz (2017b) demonstrated that an
82 unbiased image can be inverted using box tomography if the initial background model
83 is a homogenized true model (Capdeville et al., 2010) in a two-dimensional (2D) global
84 acoustic model framework. These studies provided an important theoretical foundation
85 for the practical applications of box tomography, initially demonstrating its promising

86 application prospects for probing key three-dimensional (3D) structures anywhere within
87 the Earth.

88 As the forward part of box tomography, an efficient implementation of hybrid nu-
89 merical simulation is crucial. The first step of the global wave simulation in the hybrid
90 wave simulation framework has gradually evolved from the approximated generalized ray
91 theory (GRT) calculations (Wen & Helmberger, 1998; Chen et al., 2005; L. Zhao et al.,
92 2008, 2014, 2015) to the direct solution method (DSM) (Kawai et al., 2006; Monteiller
93 et al., 2013; Y. Wang et al., 2016), planar wave approximation frequencywavenumber (FK)
94 (Zhu & Rivera, 2002; Tong, Chen, et al., 2014; Tong, Komatitsch, et al., 2014; Monteiller
95 et al., 2020), AXISEM (Nissen-Meyer et al., 2014; Beller et al., 2018; Pienkowska et al.,
96 2021; Monteiller et al., 2020), SPECSEM3D_globe (Komatitsch et al., 2002; Clouzet et
97 al., 2018), and AXISEM3D (Leng et al., 2019, 2020), owing to the large computation re-
98 sources required for 3D high-frequency wave numerical simulations at the global scale.
99 For the second step of the hybrid wave numerical simulation, a unifying theory was in-
100 troduced in Masson et al. (2014), the representation theorem being their theoretical ba-
101 sis (Wen & Helmberger, 1998; Masson et al., 2014; Lin et al., 2019). Existing hybrid-wave
102 numerical simulation methods consist of two main categories. The first one explicitly ap-
103 proximates the surface integral(s) in the physical representation theorem to build the
104 physical hybrid inputs and is referred to as the “multiple point sources method” (Chevrot
105 et al., 2004; Monteiller et al., 2013; Tong, Chen, et al., 2014; Tong, Komatitsch, et al.,
106 2014; M. Zhao et al., 2016; Y. Wang et al., 2016; Lin et al., 2019). The second category
107 constructs the numerical hybrid inputs using a spatial window function and the discrete
108 wave equation based on the numerical representation theorem and is referred to as the
109 “direct discrete differentiation method” (Bielak et al., 2003; Yoshimura et al., 2003; Mas-
110 son et al., 2014; Masson & Romanowicz, 2017b, 2017a; Clouzet et al., 2018).

111 In the research on hybrid wave numerical simulation methods, the following oper-
112 ations are vital: in the first step, reducing the memory requirements of the hybrid in-
113 puts in the global simulation; in the second step, accurately performing the hybrid nu-
114 merical simulations completely independent of the first global simulation (e.g., the ir-
115 relevant selections of spatial meshing and temporal steps) and increasing the computa-
116 tion speed of the local hybrid numerical simulations. To the best of our knowledge, no
117 previous hybrid method has combined the two main categories of hybrid simulation. The
118 proposed “new” hybrid method inherits the advantages of both main hybrid methods
119 and simultaneously eliminates their disadvantages. To save hybrid inputs, the memory
120 requirements of the proposed hybrid method and memory-saving multiple point sources
121 method are the same. To use the proposed method in the acoustic scenario, we must know

122 three incident physical quantities: the gradient, potential, and acceleration. Note that
 123 the acceleration term can be calculated using the stored potential term during the hy-
 124 brid simulation; therefore, it does not require storing. It has the advantage of being nat-
 125 urally combined with a perfectly matched layer (PML) for very heterogeneous media with-
 126 out a significant artificial error. The storage ratio between the new hybrid method and
 127 the direct discrete differentiation methods based on the numerical representation the-
 128 orem is approximately $\frac{2}{N+1}$ (N : the polynomial degree in the SEM). Therefore, it is more
 129 suitable for the hybrid numerical simulations of wave propagation, particularly for an
 130 efficient very high polynomial degree SEM (Lyu et al., 2020).

131 The remainder of this article is organized as follows. First, we illustrate the detailed
 132 expression of the fundamental representation theorem. Subsequently, two main categories
 133 of the hybrid simulation, including five different subcategories (Bielak et al., 2003; Mon-
 134 teiller et al., 2013; Masson et al., 2014; M. Zhao et al., 2016; Lin et al., 2019) are ana-
 135 lyzed, and the new hybrid method is proposed based on their combination. Thereafter,
 136 a series of 2D and 3D hybrid acoustic wave numerical simulations using SEM in homo-
 137 geneous and heterogeneous models demonstrate its validity. Finally, the discussion and
 138 conclusions are presented.

139 3 Methodology

140 In this section, we begin with the elastic and acoustic wave equations, and we briefly
 141 introduce the principles of the spectral element method and the associated representa-
 142 tion theorems. Subsequently, some nomenclature and the overall workflow of the hybrid
 143 simulation are introduced. Thereafter, we briefly analyze the widely used hybrid meth-
 144 ods, including two main categories and five subcategories, and summarize their respec-
 145 tive merits and limitations. Finally, the new hybrid method is proposed based on their
 146 combination.

147 3.1 Elastic and Acoustic Wave Equation

148 The propagation of seismic waves is governed by the equations of motion:

$$\begin{aligned}
 \rho \ddot{\mathbf{u}} &= \nabla \cdot \boldsymbol{\sigma} + \mathbf{f} \\
 \boldsymbol{\sigma} &= \mathbf{C} : \boldsymbol{\varepsilon} \\
 \boldsymbol{\varepsilon} &= \frac{1}{2} [\nabla \mathbf{u} + (\nabla \mathbf{u})^T],
 \end{aligned} \tag{1}$$

149 where $\mathbf{u}(\mathbf{x}, t)$ is the displacement field vector, $\rho(\mathbf{x})$ is the density, $\boldsymbol{\sigma}(\mathbf{x})$ is the stress ten-
 150 sor, $\boldsymbol{\varepsilon}(\mathbf{x})$ is the strain tensor, and $\mathbf{f}(\mathbf{x}, t)$ are the body forces in the elastic domain Ω ; \mathbf{u}
 151 is subject to boundary conditions on $\partial\Omega$ (i.e., traction vanishes at the Earth's surface).

152 In the acoustic scenario, considering an acoustic domain Ω , the velocity potential
153 q is the solution of

$$\begin{aligned}\frac{1}{\kappa}\ddot{q} &= \nabla \cdot \dot{\mathbf{u}} + f \\ \dot{\mathbf{u}} &= \frac{1}{\rho}\nabla q,\end{aligned}\quad (2)$$

154 where $\kappa(\mathbf{x})$ is the acoustic bulk modulus, $\rho(\mathbf{x})$ is the (mass) density, $\mathbf{u}(\mathbf{x}, t)$ is the dis-
155 placement vector, and $f(\mathbf{x}, t)$ is a scalar source term. Generally, the acoustic medium
156 is fully described using only two parameters: the density $\rho(\mathbf{x})$ and the speed of sound
157 $V(\mathbf{x})$ such that $\kappa(\mathbf{x}) = \rho(\mathbf{x})V^2(\mathbf{x})$. Note that we only tested our proposed hybrid method
158 in the acoustic scenario in the following numerical experiments.

159 **3.2 Principle of the Spectral Element Method**

160 The SEM is a finite-element type method. Rather than directly using the bound-
161 ary conditions and equations of motion, it is based on an associated weak form by dot-
162 ting the wave equation with an arbitrary test function $w(\mathbf{x})$, integrating by parts over
163 the model domain Ω , and imposing the associated boundary conditions. To numerically
164 solve the weak form of the equation, we require a discrete approximation of the contin-
165 uous problem. For the spatial discretization of the SEM, the 3D model domain Ω is spa-
166 tially split into N_e non-overlapping spectral elements. For the acoustic wave equation,
167 $q^e(\mathbf{x}) = \sum_{i,j,k=0,N+1} Q_{ijk}^e w_{ijk}^e(\mathbf{x})$ ($e = 1, \dots, N_e$), $w_{ijk}^e(\mathbf{x})$ is the $i + j \times (N + 1) +$
168 $k \times (N + 1)^2$ th test function in the e th spectral element, $q^e(\mathbf{x})$ is $q(\mathbf{x})$ restricted to the
169 e th element, the subscript N represents the polynomial degree of spectral element, and
170 Q_{ijk}^e is $q(x_{ijk}^e)$ where x_{ijk}^e is the coordinate of the $i + j \times (N + 1) + k \times (N + 1)^2$ th Gauss-
171 Lobatto-Legendre (GLL) point in the e th element. After the numerical integration based
172 on the GLL points is applied to the weak form of the above acoustic wave equation (2),
173 the following ordinary differential equation (ODE) is obtained:

$$\mathbf{M}\ddot{\mathbf{Q}} + \mathbf{K}\mathbf{Q} = \mathbf{F}, \quad (3)$$

174 where \mathbf{Q} is the discrete potential vector, \mathbf{M} is the global diagonal mass matrix, \mathbf{K} is the
175 global stiffness matrix, and \mathbf{F} is the discrete source vector (Komatitsch & Tromp, 1999).
176 Note that $\mathbf{K}\mathbf{Q}$ is calculated using the tensor product.

177 **3.3 Theoretical Basis of Hybrid Simulation: Representation Theorem**

178 Hybrid methods are often based on the representation theorem (Aki & Richards,
179 2002; Masson et al., 2014; M. Zhao et al., 2016; Lin et al., 2019). It quantitatively states
180 a manner in which displacement \mathbf{u} at a certain point \mathbf{x} consists of three contributions
181 because of the force $\mathbf{f}(\mathbf{x}, t)$ throughout the closed V , as well as contributions owing to

182 the traction $\mathbf{T}(\mathbf{u}, \mathbf{n})$ and the displacement \mathbf{u} itself on the surface $S = \partial V$.

$$\begin{aligned}
 u_n(\mathbf{x}, t) &= \int_{-\infty}^{\infty} d\tau \int_V f_i(\mathbf{x}', \tau) G_{ni}(\mathbf{x}, t - \tau; \mathbf{x}', 0) dV(\mathbf{x}') \\
 &+ \int_{-\infty}^{\infty} d\tau \oint_S T_i(\mathbf{u}(\mathbf{x}', \tau), \mathbf{n}) G_{ni}(\mathbf{x}, t - \tau; \mathbf{x}', 0) dS(\mathbf{x}') \\
 &- \int_{-\infty}^{\infty} d\tau \oint_S u_i(\mathbf{x}', \tau) C_{ijkl} n_j G_{nk,l}(\mathbf{x}, t - \tau; \mathbf{x}', 0) dS(\mathbf{x}'), \quad (4)
 \end{aligned}$$

183 where Green's tensor $G_{ni}(\mathbf{x}, t; \mathbf{x}', \tau)$ denotes the n th direction component of the displacement at (\mathbf{x}, t) owing to a unit point force at (\mathbf{x}', τ) in the i th direction, $T_i = \sigma_{ij} n_j =$
 184 $C_{ijkl} u_{k,l} n_j$ is the i th component of the traction on S , n_j is the j th component of the normal vector \mathbf{n} on S , C_{ijkl} is the fourth-order elasticity tensor, and the notation $G_{nk,l}$ represents $\frac{\partial G_{nk}}{\partial x'_l}$. The third integral in Equation (4) indicates the displacement contribution owing to the moment density tensor $m_{kl} = u_i n_j C_{ijkl}$. Note that the Einstein summation convention is used. Equation (4) indicates that if the exciting force $f_i(\mathbf{x}, t)$ is known throughout the volume V , the traction $T_i(\mathbf{x}, \mathbf{n}, t)$ and the wavefield $u_i(\mathbf{x}, t)$ are known on the surface S , then the displacement $u_n(\mathbf{x}, t)$ within the volume V can be regenerated, which is the theoretical foundation of the hybrid simulation of the elastic wave equation.
 193

194 Similar to the elastic scenario, the acoustic pressure can be expressed formally in
 195 the temporal domain using the Helmholtz–Kirchhoff representation theorem:

$$\begin{aligned}
 q(\mathbf{x}, t) &= \int_{-\infty}^{\infty} d\tau \int_V f(\mathbf{x}', \tau) G(\mathbf{x}, t - \tau; \mathbf{x}', 0) dV(\mathbf{x}') \\
 &+ \int_{-\infty}^{\infty} d\tau \oint_S \frac{1}{\rho} \nabla' q(\mathbf{x}', \tau) G(\mathbf{x}, t - \tau; \mathbf{x}', 0) \cdot \mathbf{n} dS(\mathbf{x}') \\
 &- \int_{-\infty}^{\infty} d\tau \oint_S \frac{1}{\rho} q(\mathbf{x}', \tau) \nabla' G(\mathbf{x}, t - \tau; \mathbf{x}', 0) \cdot \mathbf{n} dS(\mathbf{x}'). \quad (5)
 \end{aligned}$$

196 Equation (5) can be transferred into the frequency domain as follows (the frequency dependence of functions is omitted hereafter to avoid complexity for equations):
 197

$$\begin{aligned}
 q(\mathbf{x}) &= \int_V f(\mathbf{x}') G(\mathbf{x}; \mathbf{x}') dV(\mathbf{x}') \\
 &+ \oint_S \frac{1}{\rho} \nabla' q(\mathbf{x}') G(\mathbf{x}; \mathbf{x}') \cdot \mathbf{n} dS(\mathbf{x}') \\
 &- \oint_S \frac{1}{\rho} q(\mathbf{x}') \nabla' G(\mathbf{x}; \mathbf{x}') \cdot \mathbf{n} dS(\mathbf{x}'). \quad (6)
 \end{aligned}$$

198 Note that the same notation is used for quantities in the time and frequency domains.
 199 By replacing the surface sources with equivalent body sources (Aki & Richards, 2002),
 200 Equation (6) can be rewritten as

$$q(\mathbf{x}) = \int_V [f(\mathbf{x}') + f^T(\mathbf{x}') + f^q(\mathbf{x}')] G(\mathbf{x}; \mathbf{x}') dV(\mathbf{x}'), \quad (7)$$

201 where the two equivalent body forces associated with the gradient $\nabla q(\mathbf{x}, t)$ and the po-
 202 tential $q(\mathbf{x}, t)$ are given by

$$\begin{aligned} f^T(\mathbf{x}') &= \int_S \frac{1}{\rho} n_i \frac{\partial q}{\partial \eta_i} \delta(\mathbf{x}' - \boldsymbol{\eta}) \mathbf{d}S(\boldsymbol{\eta}) \\ f^q(\mathbf{x}') &= \int_S \frac{1}{\rho} \partial_{\eta_i} [n_i q(\boldsymbol{\eta}) \delta(\mathbf{x}' - \boldsymbol{\eta})] \mathbf{d}S(\boldsymbol{\eta}), \end{aligned} \quad (8)$$

203 where the terms $T = \frac{1}{\rho} n_i \frac{\partial q}{\partial x_i}$ and $m_i = n_i q$ are similar to the traction and moment
 204 density tensor terms in the representation theorem for elastic waves. Equation (5) in-
 205 dicates that if the exciting force $f(\mathbf{x}, t)$ is known throughout the volume V , the gradi-
 206 ent $\nabla q(\mathbf{x}, t)$ and the potential $q(\mathbf{x}, t)$ are known on the surface S , then the pressure $q(\mathbf{x}, t)$
 207 within the volume V can be regenerated. Similar to the elastic scenario, it is also the
 208 theoretical foundation of the hybrid simulation of the acoustic wave equation.

209 3.4 Nomenclature and Workflow of Hybrid Simulations

210 For a clearer statement, some nomenclature often used in the hybrid simulations
 211 are listed below and depicted in Figure 1.

- 212 • **Global domain** Ω_g : the entire physical global domain containing the local do-
 213 main Ω_l and external domain Ω_e .
- 214 • **Local domain** Ω_l : the local closed box surrounded by the hybrid interface S and
 215 located inside the global domain Ω_g .
- 216 • **External domain** Ω_e : the external part of the global domain Ω_g outside the lo-
 217 cal domain Ω_l .
- 218 • **Global reference model** M_{g0} : the known 1D model (e.g., 1D AK135 (Kennett
 219 et al., 1995)) or 3D long-period velocity model (e.g., SEMUCB-WM1 in French
 220 and Romanowicz (2014)) from previous studies assigned to the global domain Ω_g ,
 221 which includes the known external model M_{e0} and local reference model M_{l0} .
- 222 • **Global target model** M_{g1} : the global model also assigned to the global domain
 223 Ω_g , which includes the assumed known external model M_{e0} and the unknown lo-
 224 cal target model M_{l1} .
- 225 • **Local reference model** M_{l0} : the known model assigned to the local domain Ω_l ,
 226 which is always the starting model for box tomography.
- 227 • **Local target model** M_{l1} : the unknown model to be inverted for and also assigned
 228 to the local domain Ω_l .
- 229 • **External model** M_{e0} : the known external model of the global reference or tar-
 230 get model assigned to the external domain Ω_e .
- 231 • **Hybrid interface** S : the interface separating the external domain Ω_e and local
 232 domain Ω_l .

233 Note that $\Omega_e + \Omega_l = \Omega_g$ for the domains, and $M_{e0} + M_{l0} = M_{g0}$ and $M_{e0} + M_{l1} = M_{g1}$
 234 for the models. As the foundation of box tomography, the forward and backward numer-
 235 ical simulations must be exclusively re-performed in the unknown local target models
 236 M_{l1} because the external model M_e is assumed to be unperturbed in the framework of
 237 the iterative box tomography.

238 The key workflow of the hybrid simulation for forward solving the wave equation
 239 in box tomography consists of the following three main steps:

- 240 • (i) Calculate and record the associated hybrid inputs using global solvers: GRT,
 241 FK, DSM, or AxiSEM for the 1D global reference model M_{g0} (e.g., AK135), and
 242 SPECFEM3D_globe or AxiSEM3D for the 3D global reference model M_{g0} (e.g.,
 243 SEMUCB-WM1).
- 244 • (ii) Impose the hybrid inputs recorded in the first step into the local target model
 245 M_{l1} and perform the local hybrid numerical simulation using a local solver, such
 246 as the program RegSEM (Cupillard et al., 2012).
- 247 • (iii) Record the residual wavefields on the hybrid interface S and use a wavefield
 248 extrapolation method (Robertsson & Chapman, 2000) to obtain the seismic re-
 249 sponse for the receivers outside the local domain Ω_l (Masson & Romanowicz, 2017a,
 250 2017b).

251 **3.5 Multiple Point Sources Method**

252 The first major category, the multiple point sources method, primarily consists of
 253 the “VM” (abbreviation obtained from Monteiller et al. (2013)) and “RP” (abbrevia-
 254 tion for the representation theorem) hybrid methods.

255 **3.5.1 VM Hybrid Method**

256 The first popular type of the multiple point sources method is the VM hybrid method
 257 (Chevrot et al., 2004; Godinho et al., 2009; Monteiller et al., 2013; Tong, Chen, et al.,
 258 2014; Tong, Komatitsch, et al., 2014; Monteiller et al., 2015; Lin et al., 2019). The con-
 259 cept of the local target model M_{l1} associated with the VM method is shown in Figure 1c.
 260 The hybrid interface S cannot be selected at will, but it should be the same as the bound-
 261 ary of the local domain $\partial\Omega_l$ indicated by the closed dashed cyan line. The VM hybrid method
 262 is only based on a special representation theorem with the traction-free boundary con-
 263 dition, which will cause the second displacement surface integral term equal to be zero,
 264 as discussed on page 29 of the 2nd edition of Aki and Richards (2002) and Equation (12)

265 in Lin et al. (2019):

$$q(\mathbf{x}, t) = \int_{-\infty}^{\infty} d\tau \oint_S \frac{1}{\rho} \nabla' q(\mathbf{x}', \tau) G(\mathbf{x}, t - \tau; \mathbf{x}', 0) \cdot \mathbf{n} dS(\mathbf{x}'). \quad (9)$$

266 The physical hybrid input is the traction ∇q (gradient) recorded in the global reference
 267 model M_{g0} . Based on the numerical integration of Equation (9) as implemented in Equa-
 268 tion (A3), the physical hybrid input ∇q can be imposed on the boundary $\partial\Omega_l$ of the lo-
 269 cal target model M_{l1} to implement the hybrid numerical simulation (refer to Appendix
 270 A for details).

271 The VM hybrid method physically operates owing to the effect of the doubling am-
 272 plitude of the free reflection from the hybrid interface. Note that here, only the first gra-
 273 dient surface integral in Equation (6) is imposed on the hybrid interface S , and the sec-
 274 ond potential integral term is equal to zero. We can consider that a force source is im-
 275 posed at a point within the local domain, which is infinitely close to the hybrid inter-
 276 face. According to the source mechanism of the point source, the amplitudes of the two
 277 wavefronts propagating in opposite directions are the same. One wave (with the half-
 278 amplitude of the hybrid waveform) propagating towards the hybrid interface will have
 279 an equivalent free reflection after encountering the interface; it then superimposes the
 280 other wave (with the other half-amplitude of the hybrid waveform) propagating away
 281 from the hybrid interface S and into the local domain. Thus, the free reflection from the
 282 hybrid interface has the effect of doubling the amplitude, with full recovery inside the
 283 local domain Ω_l . This hybrid method does not have an external region and loses the abil-
 284 ity to use the PML.

285 For the hybrid simulation using the VM method, when the local target model M_{l1}
 286 is selected to be same as the local reference model M_{l0} , the hybrid wavefield (the wave-
 287 field of the hybrid numerical simulation in the local domain Ω_l) can be recovered by im-
 288 posing the physical hybrid inputs, for example, by using the SEM as illustrated in Equa-
 289 tion (3):

$$\mathbf{M}_0 \ddot{\mathbf{Q}}_0 + \mathbf{K}_0 \mathbf{Q}_0 = \mathbf{F}_0^T, \quad (10)$$

290 where \mathbf{Q}_0 is the reference discrete potential vector, \mathbf{M}_0 is the global mass matrix, and
 291 \mathbf{K}_0 is the global stiffness matrix assigned to the local reference model M_{l0} . \mathbf{F}_0^T is the im-
 292 posed hybrid source term, which is constructed using Equation (A3) only with the gra-
 293 dient ∇q_0 of some integration points (e.g., GLL points used in this study) exactly on the
 294 hybrid interface S . Please note that this is only applicable to the local reference model.
 295 If some perturbations are present in the local domain, then q and ∇q are not actually
 296 known on the hybrid interface S because they are different from the global simulation.
 297 Appendix B discusses the related hybrid simulation with a limited absorbing boundary

condition when the selected local target model M_{l1} is different from the local reference model M_{l0} .

Figure 2 shows the 2D wavefield in a global reference model M_{g0} ; note that the snapshots at five different time steps are superposed to simplify the diagram. Figures 4b1 and 4b2 depict the hybrid wavefield and waveforms calculated using the VM hybrid method in the local reference model M_{l0} . We observe that the VM hybrid method is sufficiently accurate. The related error was $\approx 0.01\%$ under the spatial meshing setting when the local reference model M_{l0} was adopted (Section 4.1.1). Note that Figure 4 does not use any absorbing boundary condition outside the hybrid interface.

3.5.2 RP Hybrid Method

The second type of the multiple point sources hybrid method is the RP hybrid method, which is based on the normal representation theorem (Masson et al., 2014; M. Zhao et al., 2016; Lin et al., 2019) with two nonzero surface integrals. The associated concept of the local target model M_{l1} is depicted in Figure 1d. The hybrid interface S can be freely selected, and the green part corresponds to the PML boundary domain for the local simulation. The required physical hybrid inputs include the gradient ∇q and potential q exactly on the hybrid interface for the acoustic scenarios, as shown in Equation (5). The implementation is similar to the VM method but with the full imposing of two surface integrals in Equation (6). In the local target model M_{l1} , the hybrid wavefield can be calculated using the hybrid numerical simulation:

$$\mathbf{M}_1 \ddot{\mathbf{Q}}_1 + \mathbf{K}_1 \mathbf{Q}_1 = \mathbf{F}_0^T + \mathbf{F}_0^q, \quad (11)$$

where \mathbf{Q}_1 is the discrete potential vector, \mathbf{M}_1 is the global mass matrix, and \mathbf{K}_1 is the global stiffness matrix assigned to the local target model M_{l1} . \mathbf{F}_0^T and \mathbf{F}_0^q are the imposing hybrid source terms, which can be constructed using Equations (A2), (A3), and (A4) with the gradient ∇q and potential q of integration points on a closed arbitrary hybrid interface S , as plotted in the dashed cyan line or red dashed circle in Figure 1d, similar to the red dashed circle in Figure 1a–b. In this study, we selected the GLL points exactly on a rectangular hybrid interface S (the cyan dashed line surrounding the white box depicted in Figure 1d) as the numerical integration points, whose coordinates were determined using only the meshing of the local reference model M_{l0} .

Through the theoretical proof, for a given closed local domain Ω_l , the derivation of Equation (20) in Masson et al. (2014) indicates that the two surface integrals on the hybrid interface S in the RP hybrid method will have zero contribution (exact cancellation) outside of the local target domain, because u_i^M in Equation (20) is defined in the

331 entire global domain Ω and not the local domain Ω_l . Physically, imposing a traction bound-
 332 ary condition such as Equation (A3) is equivalent to applying forces on the hybrid in-
 333 terface, whereas imposing a displacement boundary condition such as Equation (A4) is
 334 equivalent to applying moment displacement tensor sources along the hybrid interface
 335 (Lin et al., 2019).

336 The superimposed contribution of these two surface integrals with the \pm symbols
 337 is +100% inside (full recovery) and zero outside (exact cancellation). Masson et al. (2014)
 338 numerically proved it using the FDM in a local reference model M_{l0} with the spherical
 339 shaped hybrid interface, and they indicated that the contributions of the traction and
 340 displacement surface integrals are +50% and -50% outside the local domain Ω_l and +50%
 341 and +50% inside the local domain Ω_l , respectively. Slightly different from their conclu-
 342 sion, in Figure 3, we numerically prove this using the SEM in a local reference model M_{l0}
 343 but with a rectangular shaped hybrid interface. In the global domain, we observe that
 344 the two waves in Figures 3a and 3b outside the local domain individually generated us-
 345 ing the two surface integrals have opposite polarities but the same absolute amplitudes;
 346 thus, they can cancel each other outside the local domain (Figures 3c and 3d1). How-
 347 ever, the two waves in Figures 3a and 3b inside the local domain generated using the two
 348 surface integrals are complicated. Only the phases that are the same as the original P
 349 wave in Figures 3a and 3b have the same polarities and absolute amplitudes (both +50%
 350 contribution of the original P wave), but the other phases have opposite polarities and
 351 the same absolute amplitudes (Figures 3c and 3d2). The sum of the two wavefields in
 352 Figure 3a–b can recover the hybrid wavefield, as shown in Figure 3c. Therefore, the RP
 353 hybrid method can obtain the full recovery inside the local domain and with a possible
 354 external domain, has a natural ability to combine the PML.

355 Figures 4a1 and 4a2 depict the hybrid wavefield and waveforms calculated using
 356 the RP method also in the local reference model M_{l0} . We can observe that the errors
 357 of the wavefield and waveforms in the elements are almost the same as those in the VM
 358 hybrid method except for the hybrid interface elements (red elements in Figure 4a1) for
 359 the same local reference model M_{l0} . To fairly compare the simulated accuracy of the dif-
 360 ferent hybrid methods as shown in Figure 4, we do not add any absorbing boundary con-
 361 dition outside the local hybrid domain Ω_l because hybrid simulations in a local reference
 362 domain can theoretically recover the hybrid wavefield the same as the global wavefield.
 363 If the PML boundary condition is used, the hybrid interface can coincide with one side
 364 of the PML boundary domain, as indicated by the cyan dashed line for the RP hybrid
 365 method in Figure 1d.

366

3.5.3 Merits and Limitations

367

368

369

370

371

372

373

374

375

376

377

378

379

380

381

382

383

384

From the above analysis, multiple point sources methods such as the VM and RP methods only require the respective physical hybrid inputs of some integral points (e.g., GLL points around the local mesh) exactly on the hybrid interface S , which is memory-saving and suitable for the practical 3D hybrid simulations. The meshing of the local target model M_{I1} is completely independent of the meshing of the global reference model M_{g0} . The associated local hybrid simulation is flexible, resulting in the possibility of using a more efficient SEM with very high polynomial degrees (e.g., degrees 12 to 24) (Lyu et al., 2020) to reduce memory requirements, speed up the forward simulation, and use the upscale non-periodic homogenization (Capdeville & Mtivier, 2018; Lyu, Capdeville, Al-Attar, & Zhao, 2021) to improve the ability of FWI. Although classic SEM applications mostly rely on degrees 4–8 in each direction, higher degrees are often not adopted, primarily owing to the explicit meshing of mechanical discontinuities and exceedingly small available time steps. Note that in the recent homogenization method in seismology to smoothen the internal mechanical discontinuity (Capdeville et al., 2010), the smooth models used in forward/backward simulations using FWI (Lyu, Capdeville, Al-Attar, & Zhao, 2021), the computational complexity analysis of code-independent features for SEM, and the actual computation time benchmarks all make very high polynomial degrees SEM attractive and competitive (Lyu et al., 2020).

385

386

387

388

389

390

391

392

For the VM hybrid method, the adopted absorbing boundary condition (ABC) is effective in the local target model M_{I1} with small structural perturbations (Monteiller et al., 2013; Tong, Chen, et al., 2014), but it is not sufficiently accurate for the scattered tangential incidence waves in complicated local target models in the hybrid calculation (Clayton & Engquist, 1977; Xie et al., 2014). It cannot adopt the PML absorption because \mathbf{F}_{0l}^T can only be imposed on the boundary of the local domain $\partial\Omega$ but not freely inside the local target model M_{I1} in Equation (11) owing to the required doubling amplitude of the free reflection from the hybrid interface.

393

394

395

396

397

398

399

400

Although the RP method can be naturally combined with the PML absorbing condition owing to the full consideration of the representation theorem, the resultant hybrid wavefield is intrinsically inaccurate in the hybrid interface elements (red elements in Figure 4a1) in which the hybrid inputs are imposed. This is because the wavefields in the elements containing the sources are not accurate for SEM (Nissen-Meyer et al., 2007). In the framework of normal numerical simulations using SEM, recent effective sources can be used to address this problem (Capdeville, 2021). In the hybrid simulation framework, an additional layer of elements can be used to bypass its influence (Lin et al., 2019).

3.6 Direct Discrete Differentiation Method

The second major category, namely, the direct discrete differentiation method, is based on the numerical representation theorem and focuses on the discrete wave equation, primarily consisting the “BY” (abbreviation expression from Bielak et al. (2003)), “YM” (abbreviation expression from Masson et al. (2014)), and “MYM” (the modified YM) hybrid methods.

3.6.1 BY Hybrid Method

Unlike the multiple point sources method, which is explicitly based on the representation theorem, Bielak et al. (2003) and Yoshimura et al. (2003) directly operated on the discrete wave equation to obtain the numerical hybrid inputs using the FEM in the global reference model M_{g0} . Hereafter, we call it the BY hybrid method, and the associated concept of the local target model M_{l1} is depicted in Figure 1e. The detailed formulae of the equivalent seismic forces (similar to the numerical hybrid inputs) in the SEM framework are as follows (refer to Bielak et al. (2003) and Yoshimura et al. (2003) for more details):

$$\mathbf{F}_0^{\text{eff}} = -\mathbf{K}_0^{se}\mathbf{Q}_0^e + \mathbf{K}_0^{es}\mathbf{Q}_0^s, \quad (12)$$

where \mathbf{K} is the stiffness matrix, the subscript 0 means that the relevant calculations are performed in the global reference model M_{g0} , and the superscripts e and s represent GLL points located inside the external domain Ω_e and on the hybrid interface S , respectively. The key property of this numerical hybrid inputs $\mathbf{F}_0^{\text{eff}}$ involve only the submatrices \mathbf{K}_0^{se} and \mathbf{K}_0^{es} , which vanish everywhere except in a single layer (the blue part in Figure 1e and the blue elements in Figure 2) in the external domain Ω_e adjacent to the hybrid interface S . Thus, the wavefield required to calculate $\mathbf{F}_0^{\text{eff}}$ is associated with all the GLL points in the single-layer elements (referred to as the “hybrid elements”), but not only on the hybrid interface S .

The BY hybrid method is an innovative and attractive method in that a teleseismic event can be replaced equivalently by forces loaded on all the GLL points in the hybrid elements in which the numerical hybrid inputs are imposed. Note that in the BY hybrid simulation, after imposing the numerical hybrid inputs $\mathbf{F}_0^{\text{eff}}$, the remaining wavefields going outside owing to the existence of unknown heterogeneities in the local target model M_{l1} can be naturally eliminated using a suitable absorbing boundary condition (e.g., the PML boundary domain corresponding to green elements in Figure 1e). This numerical expression can obtain numerical hybrid inputs from a 3D background model for 3D local imaging with a higher resolution, namely, box tomography. However, the expression of the hybrid inputs in Equation (12) implies storing the global potentials of

all the GLL points in the single layer elements, and this requires an excessive disk usage, particularly for 3D numerical simulations (Yoshimura et al., 2003), and it might be even worse if people use the very high polynomial degrees SEM, as in Lyu et al. (2020). Note that physical quantities such as the potential/displacement of the GLL points in the hybrid elements can be interpolated from the global mesh to the local mesh, but $\mathbf{F}_0^{\text{eff}}$ cannot be precomputed in the global simulation and interpolated into a mesh different from the global mesh, because the internal force term \mathbf{KQ} is discontinuous (not smooth) between connected elements and along the hybrid interface.

3.6.2 YM Hybrid Method

Masson et al. (2014) further developed the BY method and proposed a more compact numerical hybrid method, which can accurately perform the hybrid simulation in the local target model with arbitrary shapes. Hereafter, we call it the YM method, and the associated concept of local target model M_{l1} is depicted in Figure 1e. Note that only the best scenario (the same meshing used in local and global domain, described in Section Appendix C) is plotted here to illustrate the arbitrary hybrid interface; please refer to Masson et al. (2014) for more details. The YM method can construct the mirror excitation \mathbf{F}_0^{M} (the same as the numerical hybrid inputs) with two different schemes, which relies on the spatial window function and discrete wave equation. For a local target model M_{l1} with arbitrary shapes, in the global elements crossed by the hybrid interface S , in which most GLL nodes belong to the closed local target domain Ω_l , the inner scheme, with fewer storage capacity of numerical hybrid inputs than the outer scheme, can be used to construct the numerical hybrid inputs using

$$\begin{aligned}\mathbf{F}_0^{\text{M}} &= \sum_e \left(\mathbf{W}^e \cdot \mathbf{f}^e - \mathbf{W}_e \cdot (\mathbf{K}_0^e \cdot \mathbf{Q}_0^e) + \mathbf{K}_0^e \cdot (\mathbf{W}_e \cdot \mathbf{Q}_0^e) \right) \\ &= \mathbf{W} \cdot \mathbf{f} - \mathbf{W} \cdot (\mathbf{K}_0 \cdot \mathbf{Q}_0) + \mathbf{K}_0 \cdot (\mathbf{W} \cdot \mathbf{Q}_0).\end{aligned}\quad (13)$$

In contrast, in the global elements crossed by hybrid interface S , in which most GLL nodes belong to the external domain Ω_e , the outer scheme can be used to construct the numerical hybrid inputs using

$$\begin{aligned}\mathbf{F}_0^{\text{M}} &= \sum_e \left(\mathbf{W}^e \cdot \mathbf{f}^e + (\mathbf{I} - \mathbf{W}^e) \cdot (\mathbf{K}_0^e \cdot \mathbf{Q}_0^e) - \mathbf{K}_0^e \cdot [(\mathbf{I} - \mathbf{W}^e) \cdot \mathbf{Q}_0^e] \right) \\ &= \mathbf{W} \cdot \mathbf{f} + (\mathbf{I} - \mathbf{W}) \cdot (\mathbf{K}_0 \cdot \mathbf{Q}_0) - \mathbf{K}_0 \cdot [(\mathbf{I} - \mathbf{W}) \cdot \mathbf{Q}_0].\end{aligned}\quad (14)$$

Where \sum_e denotes the assembly of all element hybrid inputs. \mathbf{Q}_0^e , \mathbf{K}_0^e and \mathbf{Q}_0 , \mathbf{K}_0 are the element and assembled potential vectors and stiffness matrices, respectively, assigned to the global model M_{g0} associated with the global domain Ω_g . The element and assembled diagonal matrices \mathbf{W}^e and \mathbf{W} are discrete window functions used to fetch the local wavefield in the local domain from the global wavefield. For example, $\mathbf{W}^e \cdot \mathbf{Q}_0^e$ and

$\mathbf{W} \cdot \mathbf{Q}_0$ are related to the element and assembled potential vectors, respectively, in the local domain Ω_l . The diagonal entries of $\mathbf{W}^e \neq 0$ represent the GLL points in the global elements crossed by the hybrid interface S , and they simultaneously belong to the local target domain Ω_l . The diagonal entries of $\mathbf{W}^e = 0$ represent all the other GLL points. Both the inner and outer schemes must record the local internal force $\mathbf{W}^e \cdot (\mathbf{K}_0^e \cdot \mathbf{Q}_0^e)$ or the complement $(\mathbf{I} - \mathbf{W}^e) \cdot (\mathbf{K}_0^e \cdot \mathbf{Q}_0^e)$ and the potential $\mathbf{W}^e \cdot \mathbf{Q}_0^e$ or the complement $(\mathbf{I} - \mathbf{W}^e) \cdot \mathbf{Q}_0^e$ in the same hybrid elements crossed by the hybrid interface S during the first global simulation. The only elements that contribute to the numerical hybrid inputs \mathbf{F}_0^M are the hybrid elements, for which the value of the window function \mathbf{W}^e evaluated at the GLL nodes is not constant. When the hybrid inputs are imposed into the blue part (the hybrid elements in SEM) shown in Figure 1e, the inner scheme adds the saved displacement first before calculating the internal force, and then subtracts the saved internal force, while the imposition of the outer scheme subtracts the displacement first and then adds the internal force (refer to Masson et al. (2014) for the detailed derivation).

For the YM method, on the outside of the hybrid interface S , an additional layer of elements is always required to impose the hybrid inputs (e.g., Figure 12b in Masson et al. (2014) and Figure 5 in Clouzet et al. (2018)). The full wavefield in the local domain Ω_l , including the hybrid interface S , can be recovered after imposing the hybrid inputs, but only the remaining scattered waves are simulated in the hybrid elements. Note that in the best scenario, as discussed in Section Appendix C, the numerical hybrid inputs of YM method are the same as those of the BY method, but their proposed methods of imposing the hybrid inputs are different. Less memory is required for the YM method because it is only related to the internal force $\mathbf{W}^e (\mathbf{K}_0^e \cdot \mathbf{Q}_0^e)$ and potential $\mathbf{W}^e \mathbf{Q}_0^e$ of the GLL points exactly on the green line in Figure 2; not the \mathbf{Q}_0^e of all the GLL points in all the hybrid elements must be stored as suggested for the BY method. However, when the local meshing differs from the corresponding global meshing, spatial interpolation is used to obtain all the displacements of the GLL points required in the hybrid elements during the first global simulation.

3.6.3 MYM Hybrid Method

However, we observe that in the YM method, the additional layer of elements surrounding the local target model (the blue region in Figure 1e and blue elements in Figure 2) is not necessary. Analogously, a new Heaviside window function can be adopted such that the diagonal values $\mathbf{W}^e = 1$ are only in the local domain Ω_l , but $\mathbf{W}^e = 0$ are both on the hybrid interface S and in the external domain Ω_e . Hereafter, we call it

500 the MYM hybrid method, and the concept of local target model M_{l1} associated with the
 501 MYM method is depicted in Figure 1f. Note that the hybrid elements of the MYM method
 502 are located inside the local domain, but the hybrid elements of the YM method are out-
 503 side the local domain selected using different window functions, as indicated by the red
 504 and blue elements, respectively, in Figure 2. We can utilize the internal forces $(\mathbf{I}-\mathbf{W}^e)\cdot$
 505 $(\mathbf{K}_0^e\cdot\mathbf{Q}_0^e)$ and $(\mathbf{I}-\mathbf{W}_0^e)\cdot\mathbf{Q}_0^e$ at the GLL points exactly on the hybrid interface S in the
 506 hybrid elements to implement the hybrid simulation, according to the outer scheme of
 507 the YM method with a new Heaviside window function, depending on the equation (14).
 508 It is not an inner scheme compared to the YM method even the hybrid elements are in-
 509 side the local domain, but more like an outer scheme of the YM method with a new Heav-
 510 iside window function. Fewer elements can be used to perform hybrid numerical simu-
 511 lations without overlapping the scattered and full wavefields. Note that the red part in
 512 Figure 1f and red elements in Figure 4c1 are the hybrid elements that are selected us-
 513 ing the new window function \mathbf{W}^e to locate inside the local target domain, and the green
 514 part corresponds to the PML domain. In the best scenario, the associated numerical hy-
 515 brid inputs are only imposed on the GLL points exactly on the cyan dashed line in Fig-
 516 ure 1f and on the green line in Figure 4c1 between the PML and hybrid elements.

517 Figures 4c1 and 4c2 depict the hybrid wavefield and waveforms of the MYM method.
 518 The resultant hybrid waveforms are perfectly accurate even when enlarged by the fac-
 519 tor of 10^{40} when the local meshing is the same as the global meshing surrounded by the
 520 green line as shown in Figure 2. The reason for the preciseness is that the MYM hybrid
 521 method depends on the numerical hybrid inputs to implement the local hybrid simula-
 522 tion. In the local simulation using the MYM method, all the potentials of the GLL points
 523 required by the equation (14) are calculated and saved during the global simulation, then
 524 a new local equation fully equivalent to the global equation inside the local reference model
 525 is compactly reconstructed. A similar numerical approach operating on the matrices of
 526 the solvers is shown in Bielak et al. (2003). We fetch the required local part of the global
 527 matrix solver; thus, they should be exactly the same. However, when the local meshing
 528 is different from the corresponding global meshing, as in the YM method, we must also
 529 use the spatial interpolation to obtain all the potentials of GLL points in the hybrid el-
 530 ements during the first global simulation. The related spatial-interpolation error will af-
 531 fect the results of the hybrid simulations to an extent.

532 **3.6.4 Merits and Limitations**

533 From the above analysis, the BY, YM, and MYM methods have certain advantages:
 534 (i) In the best scenario, only the numerical hybrid inputs of GLL points exactly on the

535 hybrid interface S are required, which is also memory-saving and very suitable for 3D
 536 hybrid simulation and is the same as the multiple point sources method. (ii) The PML
 537 can be applied naturally to the remaining scattered wave going outside, which results
 538 in an accurate hybrid simulation. The MYM method does not require an additional layer
 539 of elements outside the local target domain Ω_l . However, they are required by the BY
 540 and YM methods to impose the hybrid inputs and with only the scattered waves inside.
 541 Therefore, for the MYM method, the scattered and full wavefield do not co-exist.

542 However, the direct discrete differentiation method has a disadvantage. 1D global
 543 solvers such as the DSM tending to offer physical hybrid inputs without spatial inter-
 544 polation errors are relatively difficult to apply with the BY, YM, and MYM methods be-
 545 cause all the displacement at the GLL nodes in the hybrid elements are required to cal-
 546 culate the internal force term. For 3D global solvers such as SPECFEM3D_globe that
 547 can offer numerical hybrid inputs, for an accurate implementation of numerical hybrid
 548 inputs, the meshing of the local target model M_{l1} connected with the hybrid interface
 549 should be exactly the same as the meshing of the global reference model M_{g1} . However,
 550 when the local meshing is different from the global meshing, we must calculate all the
 551 corresponding displacements of all GLL points in the hybrid elements of the local mesh-
 552 ing using spatial interpolation and then obtain part of the hybrid inputs by calculating
 553 the tensor product \mathbf{KQ} inside the hybrid elements. These hybrid methods are all based
 554 on the numerical representation theorem; they require a large amount of storage, and
 555 they are not suitable for the efficient very high polynomial degree spectral element method.
 556 Because numerous GLL points of the hybrid elements are required to construct the nu-
 557 merical hybrid inputs (approximately $\frac{N+1}{2}$ times memory as the multiple sources method,
 558 N is the polynomial order of the adopted SEM; refer to the discussion section for de-
 559 tailed derivation), and the spatial interpolation introduces some errors, limiting its use
 560 to an extent.

561 **3.7 New Hybrid Method**

562 As the above analysis shows, the RP method can naturally adopt the PML, and
 563 their meshing connected with the hybrid interface of the local and reference model can
 564 differ from the global meshing, resulting in the possibility of adopting the more efficient
 565 SEM with very high polynomial degrees, but with the intrinsic inaccuracy in the elements
 566 where the hybrid inputs are imposed. The MYM method is capable of natural PML ab-
 567 sorption, but the memory requirement is significantly larger than the multiple point sources
 568 method particularly for the very high polynomial degrees SEM. For the VM method, the
 569 local meshing is independent of the global meshing, but it cannot adopt efficient PML

570 absorption. To obtain the essence of fewer memory requirements, flexible meshing, and
 571 natural PML absorption, and discard the dregs, such as only absorption with ABC or
 572 inaccurate simulation of the elements with sources, we develop a new hybrid method by
 573 combining the multiple point sources and direct discrete differentiation methods.

574 First, we combine the VM method in Equation (10) and MYM method in Equa-
 575 tion (14).

$$\begin{aligned}\mathbf{F}_0^T &= \mathbf{M}_0\ddot{\mathbf{Q}}_0 + \mathbf{K}_0 \cdot \mathbf{Q}_0 \\ \mathbf{F}_0^M &= \mathbf{W}\mathbf{f} - (\mathbf{I} - \mathbf{W}) \cdot (\mathbf{K}_0 \cdot \mathbf{Q}_0) - \mathbf{K}_0 \cdot [(\mathbf{I} - \mathbf{W}) \cdot \mathbf{Q}_0].\end{aligned}\quad (15)$$

576 After replacing the internal force term $\mathbf{K}_0 \cdot \mathbf{Q}_0$ in the second equation with the first equa-
 577 tion, we can obtain a new formula for the numerical hybrid inputs:

$$\mathbf{F}_0^M = \mathbf{W}\mathbf{f} - (\mathbf{I} - \mathbf{W}) \cdot (\mathbf{F}_0^T - \mathbf{M}_0\ddot{\mathbf{Q}}_0) - \mathbf{K}_0 \cdot [(\mathbf{I} - \mathbf{W}) \cdot \mathbf{Q}_0].\quad (16)$$

578 We circumvent the requirement for q at all GLL points in the hybrid elements to cal-
 579 culate the internal force term and instead use the difference between the external force
 580 term (traction term \mathbf{F}_0^T) and the inertial force term (acceleration term $\mathbf{M}_0\ddot{\mathbf{Q}}_0$). There-
 581 fore, we can utilize only three physical terms on the hybrid interface to obtain hybrid
 582 inputs. Using Equation (16), to obtain the new combined hybrid inputs \mathbf{F}_0^M , we first re-
 583 quire the gradient ∇q to construct the traction vector \mathbf{F}_0^T , as mentioned in Section 3.5.1.
 584 In addition, we require the potential q and the second temporal derivative of the poten-
 585 tial $\partial_{tt}q$ to build the numerical hybrid inputs during the first global simulation in the
 586 reference model M_{g0} . Note that in practice, we can compute \ddot{q} directly from the saved
 587 q field instead of saving them during the global simulation. These three physical quan-
 588 tities are located at the integration points (e.g., GLL) exactly on the hybrid interface
 589 S . To implement the new hybrid simulation, we can directly impose the hybrid inputs
 590 into the integration points on the hybrid interface regardless of whether the internal struc-
 591 ture is changed. We can conclude that the proposed hybrid method has the following
 592 advantages:

- 593 • The three physical quantities used to construct the hybrid inputs can be obtained
 594 flexibly using the global solver (e.g., DSM, SPECSEM3D_globe, or AxisSEM3D),
 595 and the meshing of the local target model is completely independent of the mesh-
 596 ing of the global reference model.
- 597 • Only the associated three physical quantities of the points exactly located on the
 598 2D hybrid interface are required, which is highly accurate and memory efficient

599 for the 3D hybrid numerical simulation and can increase the computational effi-
600 ciency of the box tomography.

- 601 • The efficient PML can be adopted naturally without any elements overlapping be-
602 tween the local and PML domains, which can further increase the imaging accu-
603 racy of the box tomography.

604 The concept of the local target model M_{l1} associated with the new hybrid method is de-
605 picted in Figure 1f. Figures 4d1 and 4d2 show the hybrid wavefield and waveforms of
606 the new hybrid method, and we can observe that the error of the new method is almost
607 the same as the VM method in Figure 4b2 for the same local reference model M_{g0} . How-
608 ever, as discussed in Section 3.5.1 and the numerical simulations benchmark in Section 4.1.3,
609 if the local target model is strongly heterogeneous, the VM method is not effective be-
610 cause it cannot be combined with the PML absorbing condition. The RP hybrid method
611 would be a better alternative compared with the proposed method when the traditional
612 SEM with $\text{NGLL} = 5$ is used for the box setting with the source outside and receiver
613 inside (SORI). However, if the very high polynomial degree SEM is used in the hybrid
614 simulation, and the acceleration \ddot{q} is calculated using the stored potential q during the
615 hybrid simulation, the new method will have a more efficient computation cost of the
616 local simulation and fewer memory requirements of the hybrid inputs. Note that com-
617 bining the new and RP hybrid methods is very useful for the hybrid simulations in the
618 box settings with the source inside and receiver outside (SIRO) and the source outside
619 and receiver outside (SORO). Note that a special hybrid method for separately solving
620 the PML domain and full waveform domain was implemented in Xie et al. (2014). Their
621 key concept of their hybrid method was to separate the entire domain into the diffracted
622 waveform domain and full waveform domain, and to solve them separately in two dif-
623 ferent ordinary differential equations, while our proposed method solved them in one or-
624 dinary differential equation same as the traditional solver using the spectral element method.
625 Note that the RP hybrid method theoretically results in zero contributions on the hy-
626 brid interface S when the hybrid simulation is performed in the local reference model
627 M_{l0} . We must consider the known saved potentials and the scattered potentials obtained
628 by the hybrid simulation on the hybrid interface when calculating the hybrid waveforms
629 of the stations located within the elements containing the hybrid interface. It is the same
630 for the MYM and “new” hybrid methods, but it is not required for the VM, BY, and
631 YM hybrid methods.

632 In summary, in this section, we analyze in detail the two main hybrid categories
633 and five subcategories (RP, VM, BY, YM, and MYM) of hybrid methods, and we pro-
634 pose a new hybrid method. The new hybrid method inherits the advantages of the VM

635 and MYM methods and eliminates their disadvantages. In Table 1, we compare these
 636 six hybrid methods in four criteria under 3D hybrid simulations as in Sections 4.3 and 4.4:
 637 i) physical or numerical representation theorems; ii) stored quantities in the best scenario
 638 or when the local and global meshings are different; iii) the required storage size in a 3D
 639 hybrid simulation in the best scenario or when the local and global meshings are differ-
 640 ent; iv) whether the absorbing boundary condition can be used. In the next section, we
 641 discuss a series of numerical experiments to benchmark and verify these hybrid meth-
 642 ods.

643 **4 Numerical Experiments**

644 To numerically validate the proposed hybrid method and benchmark its numer-
 645 ical accuracy with other existing hybrid methods, we set up a series of 2D and 3D nu-
 646 merical experiments in homogeneous and heterogeneous acoustic models. For the homo-
 647 geneous models, we utilized $V_{P0} = 3750$ m/s for the P-wave velocity and $\rho_0 = 2000$ kg/m³
 648 for the density. For the heterogeneous scenario, we kept the density constant, and $\kappa(\mathbf{x})$
 649 was in the form of a Gaussian or monochromatic oscillatory function. The detailed def-
 650 inition of heterogeneity was defined by a spatial function $f(\mathbf{x})$ as follows:

$$651 \kappa(\mathbf{x}) = \kappa_0 f(\mathbf{x}), \quad (17)$$

652 where $\kappa_0 = \rho_0 V_{P0}^2$.

653 For the descriptions of the model size and the time duration in the acoustic sce-
 654 nario, the maximum frequency and P-wave velocity defined the minimum wavelength of
 the propagation wavefield as

$$655 \lambda_{\min} = \frac{V_P}{f_{\max}}. \quad (18)$$

656 Subsequently, we measured the spatial scale as a function of λ_{\min} and the temporal scale
 as a function of

$$657 t_{\min} = \frac{1}{f_{\max}}. \quad (19)$$

658 The source was a point force located in the middle of the free surface, and its time wavelet
 659 was a Ricker function (the second derivative of a Gaussian) with a central frequency of
 660 $f_0 = 2$ Hz for 2D scenarios and $f_0 = 0.4$ Hz for 3D scenarios. Thus, λ_{\min} was approx-
 661 imately 625 and 3125 m in 2D and 3D scenarios, respectively. Thirteen receivers were
 662 evenly located in the local models, as shown in Figures 2 and 10a for the 2D and 3D sce-
 663 narios, respectively. In the global numerical simulations, the boundary conditions were
 664 free normal stress conditions all around the domains to fully exclude imperfect absorp-
 tion, and the selected domains were sufficiently wide to ensure that no reflected waves

	Representation theorem	Stored quantities same/different meshing	Required storage size same/different meshing	Absorbing condition
VM	physical	traction+velocity same	$2 \times 3V_1 \times nt$ $2 \times 3V_1 \times nt$	ABC type
RP	physical	traction+potential same	$2 \times 3V_4 \times nt$ $2 \times 3V_4 \times nt$	any
BY	numerical	potential same	$3V_3 \times nt$ $3V_3 \times nt$	any
YM	numerical	internal force+potential only potential	$2 \times 3V_1 \times nt$ $3V_3 \times nt$	any
MYM	numerical	internal force+potential only potential	$2 \times 3V_1 \times nt$ $3V_2 \times nt$	any
NEW	combination	traction+potential (acceleration) same	$2 \times 3V_1 \times nt$ $2 \times 3V_1 \times nt$	any

Table 1. Benchmarks of the VM, RP, BY, YM, MYM, and new hybrid methods. For a given 3D local target model buried in the deep earth with nex , ney , and nez elements with $NGLL$ points in each direction, $nax_0 = (nex - 2) \times N - 1$, $nay_0 = (ney - 2) \times N - 1$, $naz_0 = (nez - 2) \times N - 1$; $nax_1 = nex \times N + 1$, $nay_1 = ney \times N + 1$, $naz_1 = nez \times N + 1$; $nax_2 = nex \times N - 1$, $nay_2 = ney \times N - 1$, $naz_2 = nez \times N - 1$; $nax_3 = (nex + 2) \times N + 1$, $nay_3 = (ney + 2) \times N + 1$, $naz_3 = (nez + 2) \times N + 1$; $nax_4 = (nex + 2) \times N - 1$, $nay_4 = (ney + 2) \times N - 1$, $naz_4 = (nez + 2) \times N - 1$. Where $N = NGLL - 1$. The number of GLL points in a closed 2D hybrid interface is $V_1 = (nax_1 \times nay_1 \times naz_1 - nax_2 \times nay_2 \times naz_2)$. When the local and global meshings are different, the number of GLL points used to construct the numerical hybrid inputs using the MYM method is $V_2 = (nax_1 \times nay_1 \times naz_1 - nax_0 \times nay_0 \times naz_0)$; the number of $NGLL$ points used to construct the numerical hybrid inputs using the YM method is $V_3 = (nax_3 \times nay_3 \times naz_3 - nax_2 \times nay_2 \times naz_2)$, and the number of GLL points used to construct the physical hybrid inputs using the RP method is $V_4 = (nax_3 \times nay_3 \times naz_3 - nax_4 \times nay_4 \times naz_4)$, because one layer of elements inside the hybrid interface are needed to ensure simulated accuracy. nt is the number of time steps in the simulation without temporal interpolation. For example, the storage size of the VM is $2 \times 3V_1 \times nt$, where 2 represents the items including traction and velocity, and 3 indicates three directions in 3D. For the absorbing condition, ABC is a type of absorbing boundary-type condition, e.g., Clayton and Engquist (1977). Note that for the new method, \ddot{q} is calculated directly from the saved q field to decrease the amount of storage.

665 from boundaries affected the results. The simulated duration and temporal step Δt were
 666 $90 t_{\min}$ (15 s), 0.002 s for 2D scenarios, and $24 t_{\min}$ (20 s), 0.01 s for 3D scenarios.

667 One of the key parameters when using the SEM is G (the number of grid points
 668 per minimum wavelength). Classic SEM applications mostly rely on degrees 4–8 spec-
 669 tral elements in each tensorial direction, and the G for a high degree 20 is approximately
 670 half of that necessary for a degree 4 (Lyu et al., 2020). The commonly admitted G to
 671 obtain sufficient accuracy in a constant-velocity medium is approximately $G \approx 5$ for one
 672 element with degree 8 (NGLL = 9, number of GLL points per element per direction) (Basabe
 673 & Sen, 2007; Seriani & Oliveira, 2008; Lyu et al., 2020). A low G can be important in
 674 the FWI context owing to the extensive operations on forward and adjoint wavefields
 675 (Komatitsch et al., 2016; Lyu, Capdeville, Al-Attar, & Zhao, 2021). In our study, the
 676 meshing based on NGLL = 8 was adopted for the first global simulations in the global
 677 reference model M_{g0} . A different meshing with NGLL = 20 was used for the VM, RP,
 678 and new hybrid simulations in the local reference models M_{l0} and target models M_{l1} on
 679 account of the efficiency of very high polynomial degree SEM (Lyu et al., 2020).

680 **4.1 2D Homogeneous Global Reference Model**

681 For 2D homogeneous scenarios, the size of the global reference model M_{g0} was 160
 682 $\times 80 \lambda_{\min}^2$, which was assigned to a rectangular global domain Ω_g . The domain Ω_g and
 683 wavefields overlapping at five time steps associated with the 160×80 structural spec-
 684 tral elements with NGLL = 8 ($G = 8$) are plotted in Figure 2.

685 **4.1.1 Hybrid Simulation for a Local Reference Homogeneous Model**

686 The size of the adopted local reference model M_{l0} was $80 \times 40 \lambda_{\min}^2$, which was as-
 687 signed to the rectangular local domain Ω_l surrounded by the closed green line in Fig-
 688 ure 2 (hybrid interface S), and it was located at the center of the global reference model.
 689 The related wavefield snapshots at the same time steps as the global simulation asso-
 690 ciated with 20×10 elements with NGLL = 20 ($G = 5$) are shown in Figures 4a1, b1,
 691 and d1, which correspond to the RP, VM, and new hybrid methods, respectively. They
 692 all had the characteristics of flexible meshing, namely, the number of elements or/and
 693 the internal degree of the local meshing for the hybrid simulation differed from the re-
 694 lated global meshing of the local domain Ω_l . In comparison, the MYM method adopted
 695 local meshing with 80×40 elements with NGLL = 8 ($G = 8$), which was identical to
 696 the global meshing (Figure 4c1). A comparison of wavefields and waveforms indicated
 697 that the MYM method had no error relative to the global simulation shown in Figures 4c1
 698 and 4c2. The relative error of the RP method in the elements in which hybrid inputs were

699 imposed was very large ($\approx 10\%$) owing to the intrinsic inaccuracy of the source elements
 700 in the SEM (Figures 4a1 and 4a2). The relative errors of the VM and new methods were
 701 almost the same ($\approx 0.01\%$) (Figures 4b1, 4b2, 4d1, and 4d2), which originated from the
 702 boundary reflection of the spatial-dispersion error difference of the global and local mesh-
 703 ing. Through the hybrid numerical simulations using the RP, VM, MYM, and new meth-
 704 ods in the same 2D global and local homogeneous reference model, we initially demon-
 705 strated that the accuracy of the new method is the same as that of the VM method, but
 706 as discussed in Section 3.5.1, if the local target model is strongly heterogeneous, the VM
 707 method is not effective because it cannot be combined with the PML boundary condi-
 708 tion. Here, the MYM method is more accurate.

709 *4.1.2 Hybrid Simulation for a Local Weak Gaussian Heterogeneous Model*

710 To validate the applicability of the new hybrid method in the 2D weak heteroge-
 711 neous model, the combined hybrid inputs obtained in the 2D homogeneous reference model
 712 were imposed into the local target model M_{l1} with a Gaussian heterogeneity inside. The
 713 adopted 2D Gaussian spatial function $f(\mathbf{x})$ was

$$f(\mathbf{x}) = 1 + ae^{-\frac{\mathbf{x}^2}{2\sigma^2}}, \quad (20)$$

714 where a is the amplitude value that controls the range of $\kappa(\mathbf{x})$, and σ is the spatial scale
 715 parameter. Here, we used $a = -0.2$ and $\sigma = 2 \lambda_{\min}$ to construct a global Gaussian model,
 716 and the Gaussian heterogeneity existed only in the local domain Ω_l . The external model
 717 M_e was the same as the homogeneous reference model M_{g0} (Figure 5a).

718 Figure 5b shows the hybrid wavefield by imposing the hybrid inputs calculated in
 719 the 2D homogeneous reference model into the global Gaussian (target) model M_{g1} . The
 720 hybrid inputs can be considered new equivalent sources to replace the remote source to
 721 obtain the same wavefield in the local domain. Note that the meshing used in Figure 5b
 722 was constructed using 64×32 elements with $\text{NGLL} = 20$ ($G = 5$), different from the
 723 global meshing (160×80 elements with $\text{NGLL} = 8$ ($G = 8$)), which was used for cal-
 724 culating the global waveforms in the Figure 5d. In this scenario, the remaining scattered
 725 waves going outside were observed owing to the presence of the local Gaussian hetero-
 726 geneous anomaly. Because these waves were not part of the original reference wavefield,
 727 they were not cancelled out when they crossed the hybrid interface S , and some resid-
 728 ual wavefield leaked out of the local target model M_{l1} (Figure 5b). We could shrink our
 729 model and utilize the PML to absorb the scattered waves (Figure 5c). In the hybrid sim-
 730 ulations shown in Figures 5b and 5c, after the wavefront across the Gaussian heterogene-
 731 ity with lower velocity than the reference, it propagated more slowly than the reference
 732 wavefront in the 2D homogeneous model. Additionally, it could be observed from the

733 waveforms of the three center receivers (Figure 5d). Note that the global waveforms in
 734 Figure 5d were calculated using the 160×80 elements meshed with $\text{NGLL} = 8$ ($G =$
 735 8). Figure 5d shows that the global waveforms calculated in the model of Figure 5a and
 736 the first hybrid waveforms obtained in Figure 5b without PML absorbing condition were
 737 almost equal. The relative error was $\approx 0.01\%$, the same level as the homogeneous sce-
 738 nario. The consistency of waveforms between the first hybrid simulation (dashed red)
 739 in Figure 5b and the second hybrid simulation (solid blue) with PML absorption in Fig-
 740 ure 5c indicated that the new hybrid method can be combined with the PML absorb-
 741 ing condition naturally to absorb the remaining scattered waves going outside with a lo-
 742 cal meshing different from the global one. Please note that the structure of the PML el-
 743 ements should be selected to be the same as the one around the local reference domain
 744 in the global reference model M_{g0} , and it could not be changed during the box tomog-
 745 raphy.

746 **4.1.3 Hybrid Simulation for a Local Strong Gaussian Heterogeneous Model**

747 To validate the applicability of the new hybrid method in the 2D strongly hetero-
 748 geneous model, the hybrid inputs that were obtained in the 2D homogeneous reference
 749 model were imposed into the local target model M_{l1} with a strong Gaussian heterogene-
 750 ity inside. Here, we used $a = -0.8$ and $\sigma = 2 \lambda_{\min}$ to construct a global Gaussian model.
 751 The parameters of the meshing were the same as those in the weak scenario. Figure 6a
 752 shows the hybrid wavefield using the VM hybrid method. The hybrid inputs were cal-
 753 culated in the 2D homogeneous reference model. It was clear that the wavefront was severely
 754 deformed after passing through the low velocity. The relative waveform error of using
 755 the VM method was approximately 7.5% (Figure 6b), and the relative waveform error
 756 of using the new method was approximately 0.89% (Figure 6c) but with more calcula-
 757 tion time owing to the use of the PML absorbing condition.

758 To further verify the applied scope of the proposed hybrid method, we further tested
 759 it in 2D heterogeneous, 3D homogeneous, and heterogeneous reference models M_{g0} .

760 **4.2 2D Global Heterogeneous Reference Model**

761 For the 2D heterogeneous scenario, the size of the 2D global heterogeneous refer-
 762 ence model M_{g0} was the same as that of the 2D homogeneous scenario. The adopted 2D
 763 cosine spatial function $f(\mathbf{x})$ was defined as follows:

$$\begin{aligned} f(\mathbf{x}) &= 1 + a \left(\cos\left(\frac{2\pi}{\lambda_h} \mathbf{k}_a \cdot \mathbf{x}\right) + \cos\left(\frac{2\pi}{\lambda_h} \mathbf{k}_b \cdot \mathbf{x}\right) \right) \\ \mathbf{k}_a &= (\cos(t_1), \sin(t_1)) \end{aligned}$$

$$\mathbf{k}_b = (\cos(t_2), \sin(t_2)) \quad (21)$$

where a is the amplitude value, and t_1, t_2 are the included angles between the two heterogeneities and the x-axis. In this scenario, we used $a = \frac{1}{20}$ and $t_1 = \frac{\pi}{4}, t_2 = \frac{3\pi}{4}$ (in radians) related to two orthogonal directions (Figure 7a); $\lambda_h = \lambda_{\min}$ corresponds to a typical geological model (Capdeville et al., 2010).

Figure 7b shows the global domain Ω_g and the wavefield snapshot at $67.2 t_{\min}$ associated with 240×120 elements meshed with $\text{NGLL} = 8$ ($G = 12$, 1.5 times as the homogeneous scenario based on the empirical value in Lyu et al. (2020)). The local domain Ω_l and wavefield snapshot at the same time step associated with 30×15 elements meshing with $\text{NGLL} = 20$ ($G = 7.5$), for the scenario $\lambda_h = \lambda_{\min}$, are depicted in Figure 7c. The agreement between the hybrid and reference waveforms from the 13 receivers is shown in Figure 7d, demonstrating the effectiveness of the new hybrid method in the 2D heterogeneous global reference model M_{g0} .

We know that in actual hybrid applications, there are three types of source and receiver settings: the first one is the box with the SORI, the second one is the reverse with the SIRO, and the third is a box with the SORO. All the above-mentioned 2D hybrid simulations corresponded to the first SORI setting. In the following, we discuss how to perform the other two types of hybrid simulations by adopting the suitable hybrid method(s).

4.2.1 Hybrid Simulation with a Source Inside and a Receiver Outside

For a local hybrid simulation in the SIRO setting, the workflow has three steps: i) perform a local numerical simulation by loading the internal source in the local target model, and record the physical quantities gradient and potential terms (physical quantities needed by the representation theorem) of the GLL points on the hybrid interface; ii) perform a global numerical simulation using a single force at the location of the receiver, and record the Green's function and its gradient of the GLL points on the hybrid interface; iii) apply a quadrature rule to discretize the two surface integrals in the representation theorem (Equation 5), perform the convolution at each integral point (e.g., GLL points), and sum the contributions from all the integral points as follows.

$$\begin{aligned} q(\mathbf{x}, t) &= \int_{-\infty}^{\infty} d\tau \left(\oint_{S_f} - \oint_S \right) \frac{1}{\rho} \nabla' q(\mathbf{x}', \tau) G(\mathbf{x}, t - \tau; \mathbf{x}', 0) \cdot \mathbf{nd}S(\mathbf{x}') \\ &\quad - \int_{-\infty}^{\infty} d\tau \left(\oint_{S_f} - \oint_S \right) \frac{1}{\rho} q(\mathbf{x}', \tau) \nabla' G(\mathbf{x}, t - \tau; \mathbf{x}', 0) \cdot \mathbf{nd}S(\mathbf{x}') \\ &= 0 - \Delta t \sum_e \sum_{p=1}^{N_s} \alpha_{e,p} \left(\text{conv} \left(\frac{1}{\rho_p} n_j \partial_j q(\mathbf{x}_p, t), G(\mathbf{x}_p, t) \right) - \text{conv} \left(\frac{1}{\rho_p} q(\mathbf{x}_p, t), n_j \partial_j G(\mathbf{x}_p, t) \right) \right). \end{aligned} \quad (22)$$

791 Where the first 0 means the zero contribution from the free surface S_f ($\nabla'q$ and $\nabla'G$
 792 are equal to zero), the first summation is assembled over all the surface elements e of the
 793 hybrid interface S , and the second one is over all the quadrature points \mathbf{x}_p^e ($p = 1, \dots, N_s$),
 794 N_s is the total number of quadrature points on one surface element with the related quadra-
 795 ture weight α_p , and $\text{conv}(f(t), g(t))$ is the convolution between two time series $f(t)$ and
 796 $g(t)$.

797 The ordering of steps i) and ii) can be changed. It is worth noting that, in this SIRO
 798 setting, the stations are always located far from the hybrid interface, and we can explic-
 799 itly adopt the representation theorem by using the traction and potential terms obtained
 800 from the local simulation from the source side and using the Green's function and its gra-
 801 dient obtained from the global simulation from the receiver side. We propose not to adopt
 802 the new hybrid method in this SIRO setting.

803 Figure 8a shows an example of the 2D hybrid wavefield related to the calculation
 804 of Green's function at time step 72 t_{\min} from the receiver side, corresponding to step ii).
 805 Note that there are some stripes in Figures 8a and 9a (setting SORO); these are because
 806 the adopted spatial meshing could not accurately simulate the wavefield with the delta
 807 source time function for the calculation of the Green's function. Please note that high
 808 frequency stripes abovementioned can be implicitly filtered out by the convolution be-
 809 tween the Green's function with unlimited frequency band and the forward field with
 810 limited frequency band obtained from the banded source. In Figure 8b, the waveform
 811 benchmarks are listed. The waveform was explicitly calculated using the convolution of
 812 the representation theorem, and it had a very good consistency with the waveform cal-
 813 culated in the global reference model.

814 **4.2.2 Hybrid Simulation with a Source Outside and a Receiver Outside**

815 For a remote local target domain in the SORO setting, the workflow has the fol-
 816 lowing four steps: i) perform a numerical simulation in the global reference model from
 817 the remote source side, as in the first step in the SORI setting, and record the traction,
 818 potential, and acceleration terms of the GLL points on the hybrid interface required by
 819 the new hybrid method; ii) perform a numerical simulation in the global reference model
 820 from the remote receiver side using a single force, and record the Green's function and
 821 its gradient of the GLL points on the hybrid interface; iii) perform a hybrid numerical
 822 simulation using the new hybrid method in the local target model by imposing the hy-
 823 brid inputs recorded in step i), and record the residual traction and residual potential
 824 of the GLL points on the hybrid interface; iv) apply a quadrature rule to discretize the
 825 two surface integrals in the representation theorem (Equation 5), perform the convolu-

tion at each integral point (GLL points), and sum the contributions from all the integral points. Note that the convolutions are explicitly calculated between the residual traction and potential from step iii) and Green's function and its gradient from step (ii). We propose adopting the new hybrid method and representation theorem together in the SORO setting.

Figure 9a shows the 2D hybrid wavefield related to the calculation of Green's function in step ii) at time step 72 t_{\min} for the SORO setting. Because the distance between source and receiver was larger, the duration was 17 s ($102 t_{\min}$) in this scenario. In Figure 9b, the waveforms benchmark are listed. The black line is the waveform difference between the global waveforms respectively calculated in the global weak Gaussian model in Figure 5 and the reference model in Figure 2, and it had a very good consistency with convoluted waveform. Note that the residual traction and potential were nonzero owing to the local Gaussian heterogeneity. It is also worth noting that in the SORO setting when the local model contained the nonzero local perturbation, the combined contribution of the two surface integrals to the waveform of the remote receiver were nonzero, and it is only the scattered waveform; and when the local target model was the same as the local reference model M_{l0} without any local perturbation, the combined contribution of the two surface integrals to the waveform of the remote receiver were zero, not the full waveform.

4.3 3D Global Homogeneous Reference Model

For the 3D homogeneous scenario, the size of the 3D global homogeneous reference model M_{g0} was $32 \times 32 \times 16 \lambda_{\min}^3$. Figure 10a shows the global domain Ω_g and the wavefield snapshot at time step 15.6 t_{\min} associated with $32 \times 32 \times 16$ elements meshed with NGLL = 8 ($G = 8$). The local domain Ω_l for the hybrid simulation was also a parallelogram located at the center of the global reference domain with a half-size of $16 \times 16 \times 8 \lambda_{\min}^3$. The hybrid wavefields at the same time step associated with $4 \times 4 \times 2$ elements with NGLL = 20 ($G = 5$) are depicted in Figure 10b. The agreement between the hybrid and reference waveforms from the 13 receivers is depicted in Figure 10c, initially presenting the effectiveness of the new hybrid method in the 3D global homogeneous reference model M_{g0} .

4.4 3D Global Heterogeneous Reference Model

Finally, we performed a hybrid numerical simulation using the 3D cosine heterogeneous model shown in Figure 11a. The size of the global heterogeneous model M_{g0} was the same as in the 3D homogeneous scenario. The 3D cosine spatial function $f(\mathbf{x})$ was

860 adopted as follows:

$$\begin{aligned}
 f(\mathbf{x}) &= 1 + a \left(\cos\left(\frac{2\pi}{\lambda_h} \mathbf{k}_a \cdot \mathbf{x}\right) + \cos\left(\frac{2\pi}{\lambda_h} \mathbf{k}_b \cdot \mathbf{x}\right) + \cos\left(\frac{2\pi}{\lambda_h} \mathbf{k}_c \cdot \mathbf{x}\right) \right) \\
 \mathbf{k}_a &= (\cos(t_{11})\cos(t_{12}), \cos(t_{11})\sin(t_{12}), \sin(t_{11})) \\
 \mathbf{k}_b &= (\cos(t_{21})\cos(t_{22}), \cos(t_{21})\sin(t_{22}), \sin(t_{21})) \\
 \mathbf{k}_c &= (\cos(t_{31})\cos(t_{32}), \cos(t_{31})\sin(t_{32}), \sin(t_{31})),
 \end{aligned} \tag{23}$$

861 where a is the amplitude value, and (t_{11}, t_{12}) , (t_{21}, t_{22}) , (t_{31}, t_{32}) are the included an-
 862 gles between the three heterogeneities along the x- and y-axes, respectively. Here, we used
 863 $a = \frac{1}{30}$ and $(t_{11} = 0, t_{12} = 0)$, $(t_{21} = 0, t_{22} = \frac{\pi}{2})$, $(t_{31} = \frac{\pi}{2}, t_{32} = \frac{\pi}{2})$ corresponding
 864 to three orthogonal directions shown in Figure 11a, and $\lambda_h = \lambda_{\min}$ was adopted, cor-
 865 responding to a typical geological model (Capdeville et al., 2010). The global domain
 866 Ω_g and the wavefield snapshot at time $15.6 t_{\min}$ associated with $48 \times 48 \times 24$ elements
 867 meshed with NGLL = 8 ($G = 12$, 1.5 times of the 3D homogeneous scenario based on
 868 the empirical value in Lyu et al. (2020)) are depicted in Figure 11b. The local reference
 869 model M_{l0} was located at the center of the global domain Ω_g with a half-size of $16 \times$
 870 $16 \times 8 \lambda_{\min}^3$. The hybrid wavefield at the same time step and the local domain Ω_l as-
 871 sociated with $6 \times 6 \times 3$ elements with NGLL = 20 ($G = 7.5$, 1.5 times the 3D homo-
 872 geneous scenario) are depicted in Figure 11c. The agreement between the hybrid and ref-
 873 erence waveforms shown in Figure 11d demonstrated the effectiveness of the new hybrid
 874 method in the 3D global heterogeneous reference model, indicating a significant appli-
 875 cation prospect in probing the key 3D structures in the deep earth using box tomogra-
 876 phy.

877 5 Discussion

878 5.1 Spatial and Temporal Interpolations

879 In the 3D numerical simulations of wave propagation, dividing the minimum sam-
 880 pling points per minimum wavelength G by 2 implies a storage requirement of the hy-
 881 brid inputs divided by 4 because of the 2D planar distribution, which is significant for
 882 decreasing the memory requirements. For example, for the spatial interpolation in our
 883 3D homogenous scenario, $G = 8$ in the local simulation resulted in the storage of the hy-
 884 brid inputs being 1.6^2 times that of $G = 5$ in the local simulation (the 3D homogeneous
 885 scenario). Moreover, the computation time with degrees 12-24 can be up to twice as fast
 886 as the classic degree 4 (Lyu et al., 2020). Considering a 3D hybrid local simulation, the
 887 corresponding hybrid inputs are a 2D planar distribution; thus, the storage demand of
 888 the hybrid inputs of degree 20 ($G = 2.5$) is a quarter of that of degree 4 ($G = 5$).

889 A low G can also be very important in the FWI context because of the kernel oper-
890 eration on the partial, compressed, or full storage of the forward and adjoint wavefields
891 (Komatitsch et al., 2016; Boehm et al., 2016; Fichtner et al., 2009; Lyu, Capdeville, Al-
892 Attar, & Zhao, 2021). For the proposed hybrid method, during the first global simula-
893 tion, the physical quantities ∇q , q , and $\partial_{tt}q$ are calculated and recorded to construct the
894 combined hybrid inputs for the hybrid simulation. The flexible meshing in the local tar-
895 get model can differ from the meshing of the global model, resulting in the possibility
896 of using a low G of the hybrid inputs and the associated hybrid simulation with a very
897 high polynomial degree SEM. When the local and global meshings are different, spatial
898 Lagrange interpolation can be adopted to obtain the physical quantities of GLL points
899 exactly on the hybrid interface during the first global simulation. If the global or local
900 meshing is not sufficiently accurate, different spatial dispersion errors will be introduced
901 into the local simulation, resulting in inaccurate waveforms. Note that physical quan-
902 tities such as the potential/displacement of the GLL points for constructing the hybrid
903 inputs can be interpolated from the global to the local mesh. However, the internal force
904 term \mathbf{KQ} cannot be pre-computed in the global simulation and interpolated on a dif-
905 ferent mesh from the global mesh, because the internal force term is discontinuous be-
906 tween hybrid elements. Note that Monteiller et al. (2020) also describes that the spa-
907 tial and temporal interpolation schemes are key to increasing the efficiency of the algo-
908 rithms in the global hybrid simulation.

909 In addition to the spatial interpolation using different local meshing with a low G ,
910 we can further adopt different temporal interpolations. The hybrid inputs of the pro-
911 posed hybrid method are entirely based on the physical quantities ∇q , q , and $\partial_{tt}q$ of the
912 integration points (for example, here we used GLL points), which are localized exactly
913 on the hybrid interface S of the local target model M_{g1} . During the first global simu-
914 lation, we should be able to record them at the Nyquist sampling time steps, and then
915 the physical quantities can be recovered (interpolated) according to the time step dy-
916 namically determined using the local structures after imposing the recorded physical quan-
917 tities and before starting the hybrid simulation. Thus, combining the spatial and tem-
918 poral interpolations should significantly reduce the memory required for hybrid numer-
919 ical simulations by several tens of orders of magnitude. If different global and local time
920 steps are adopted, different temporal dispersion errors will be introduced into the local
921 simulation, resulting in inaccurate waveforms to an extent. Note that the spatial and tem-
922 poral dispersion errors have been proven to be irrelevant (Koene et al., 2018; Lyu, Capdev-
923 ille, Lu, & Zhao, 2021), which provides a theoretical basis for eliminating the temporal
924 dispersion errors in the global and hybrid simulations.

5.2 Numerical cost

To use the proposed method, we must know three incident fields (the gradient, potential, and acceleration), with the advantage of being able to use the PML in the scenario of very heterogeneous media without much artificial error owing to incomplete absorption. From the benchmark of different hybrid methods in Table 1, the storage between the new hybrid method and VM or RP hybrid methods is the same whether the local and global meshings are the same, because the \vec{q} can be obtained from the stored q field. Generally, the local and global meshings are always different because the local and global solvers are different, and the corresponding storage ratio between the new hybrid method and BY or YM hybrid methods is expressed as follows:

$$\frac{2 \times 3V_1}{3V_3} = \frac{2 \times V_1}{V_3} \approx < \frac{2}{N+1}, \quad (24)$$

because $V_3 \approx > (N+1) \times V_1$. The ratio between the new hybrid way and MYM hybrid methods is expressed as follows:

$$\frac{2 \times 3V_1}{3V_2} = \frac{2 \times V_1}{V_2} \approx > \frac{2}{N+1}, \quad (25)$$

because $V_2 \approx < (N+1) \times V_1$. Thus, for the very high polynomial degrees SEM such as $N = 20$ in the 3D scenarios, the proposed hybrid method requires significantly fewer memory requirements than the BY, YM, and MYM hybrid methods.

To build a clear work flow, we always must i) determine the coordinates of the hybrid GLL points in the local domain required using different hybrid methods; ii) calculate and record the physical quantities of the recorded hybrid GLL points during the first global forward simulation, such as the potential/displacement for YM method; iii) impose the hybrid inputs into the local model to perform the local hybrid simulation at each time step. According to the expressions of different hybrid inputs of the six listed hybrid methods (Table 1), the methods of imposing the hybrid inputs are different. At each time step, the VM method explicitly implements the traction surface integral with the integrated GLL points on the hybrid interface based on Equation (A3). The RP method requires an additional term by further explicitly implementing the second potential/displacement surface integral based on Equation (A4). The new method first implements the traction surface integral as the VM method, then directly add the potential/displacement before calculating the internal force terms, and finally directly subtracts the recorded reference acceleration from the acceleration in the target local model based on Equation (16). The BY, YM, and MYM hybrid methods are performed almost the same. The MYM hybrid first directly adds the potential/displacement to the hybrid GLL points on the hybrid interface before calculating the internal force, then calculates the internal force using the elemental stiffness matrix and the potential/displacement of all the GLL points in the

958 hybrid elements, and finally subtracts the calculated internal force from the internal force
959 in the target model based on Equation (14). The YM and BY methods use opposite steps
960 based on Equation (13). The different hybrid methods were designed to perform the hy-
961 brid simulation; however, the numerical complexity of the SEM solvers is primarily dom-
962 inated by the calculation of the internal forces (the product between the elemental stiff-
963 ness matrix and displacement vector) (Deville et al., 2002), and the imposing of hybrid
964 inputs using different hybrid methods into the local SEM solver does not change the main
965 computation part, because the number of hybrid elements is significantly lower than the
966 total number of elements in the local domain.

967 **5.3 Hybrid Inputs Obtained from Programs SPECSEM3D_globe and** 968 **AxiSEM3D for Box Tomography**

969 Box tomography has been used to image the upper-mantle shear velocity structure
970 beneath the North American continent down to a 40 s period (Clouzet et al., 2018). Their
971 hybrid inputs are calculated by the program SPECSEM3D_globe (Komatitsch et al., 2002)
972 for the seismic events outside the box based on the YM hybrid method. There is noth-
973 ing that prevents one from using the new hybrid method to obtain the hybrid inputs in
974 the framework of SPECSEM3D_globe. Alternatively, with two to three orders of mag-
975 nitude faster, the program AxiSEM3D (Leng et al., 2019) is an excellent and efficient
976 candidate solver for calculating the hybrid inputs in an existing 3D global reference model.
977 Subsequently, hybrid simulations can be implemented with a local solver (e.g., RegSEM
978 (Cupillard et al., 2012)). It is also worth emphasizing that the global solver, which is used
979 to provide the hybrid inputs, only requires to calculate the physical quantities displace-
980 ment, acceleration, and strain (for the elastic scenario) of the integration (e.g., GLL) points
981 located exactly on the hybrid interface. The local solvers used for the hybrid numeri-
982 cal simulations only require to read in these physical hybrid inputs as equivalent virtual
983 sources. There are no other connections between these two programs; therefore, the pro-
984 posed hybrid method is highly accurate and memory efficient for implementing hybrid
985 simulations in actual applications. Note that the proposed hybrid method, similar to Monteiller
986 et al. (2013) and Masson et al. (2014), cannot recover second- or higher-order scattered
987 waves, but first-order scattered waves are always stronger and more important for imag-
988 ing.

989 **6 Conclusion**

990 By analyzing and combining the respective advantages of the existing two main cat-
991 egories and five subcategories of hybrid methods, a new hybrid method is proposed. Only

992 three physical quantities, including ∇q , q , and $\partial_{tt}q$, must be obtained during the first
993 global simulation to construct the hybrid inputs, and the meshing of the local target model
994 is not limited by global meshing. Furthermore, only the associated physical quantities
995 of the integration points that are located exactly on the hybrid interface are required,
996 which is highly accurate and memory efficient for the 3D local hybrid simulation. The
997 required memories of hybrid inputs can be further reduced fourfold if the very high poly-
998 nomial degree spectral element method is used for the local hybrid simulation. Finally,
999 the more efficient absorbing boundary condition PML can be adopted naturally with-
1000 out any elements overlapping between the local and PML domains. All these characters
1001 can increase the imaging resolution and accuracy of box tomography. After theoretical
1002 analysis and numerical experiments, the consistencies of the wavefield and waveform be-
1003 tween the global and hybrid numerical simulations in 2D/3D homogeneous and hetero-
1004 geneous models validate our proposed hybrid method, indicating a significant applica-
1005 tion prospect in probing the key 3D structures in the deep Earth using box tomography.

1006 It should also be noted that this study focused only on the acoustic scenario by SEM.
1007 However, the proposed concept is general and can be adopted by other numerical meth-
1008 ods such as FDM or FEM, and it can be directly applied to studying the hybrid numer-
1009 ical simulation of both the elastic wave equation and solid–fluid coupling, or Maxwell’s
1010 equations.

1011 **Acknowledgments**

1012 First, the authors would like to acknowledge Barbara Romanowicz and Sevan Adourian
1013 from the University of California, Berkeley, for their comments on the detailed discus-
1014 sions on box tomography. The authors are grateful to all the participants in the HIWAI
1015 project for many discussions on computational seismology. The authors also thank the
1016 working environment support during the writing from the Beijing Baijiatuan Earth Sci-
1017 ence National Observation and Research Station, Beijing, China, 100095. We appreci-
1018 ate the editors Michael Bostock and Sebastien Chevrot, and the reviewer Qinya Liu and
1019 the anonymous reviewer for their useful comments that improved the manuscript. This
1020 study was supported by the National Nature Science Foundation of China (grant nos.
1021 41625016, 41888101, and 42004045), the China Scholarship Council (File No. 201804910289),
1022 and the French National Research Agency (ANR-16-CE31-0022-01, 2016-2021). We note
1023 that there are no data-sharing issues because all of the numerical parameter informa-
1024 tion is provided in the figures produced by solving the global and local hybrid numer-
1025 ical simulations in this study. Data are available at the following site: [https://doi.org/
1026 10.6084/m9.figshare.14559666.v1](https://doi.org/10.6084/m9.figshare.14559666.v1).

Appendix A Discretization and Interpolation of Traction and Moment-Density Tensor Sources in SEM in the Acoustic Model

Let us assume a quadrature rule applied to discretize the surface integral for a function $g(\mathbf{x})$:

$$\int_S g(\mathbf{x})dS \approx \sum_e \sum_{p=1}^{N_s} \alpha_p g(\mathbf{x}_p^e), \quad (\text{A1})$$

where the first summation is assembled over all the surface elements e of the hybrid interface S , and the second one is over all the quadrature points \mathbf{x}_p^e ($p = 1, \dots, N_s$), N_s is the total number of quadrature points on one surface element with the related quadrature weight α_p . Subsequently, after introducing the discretization of Equation (A1) into the two surface integrals in Equation (8), the equivalent body force expression of equation (7) can be discretized as

$$q(\mathbf{x}) = \sum_e \sum_{p=1}^{N_s} \alpha_p \int_V \{T(\mathbf{x}_p^e)\delta(\mathbf{x}' - \mathbf{x}_p^e) + \partial_i[m_i(\mathbf{x}_p^e)\delta(\mathbf{x}' - \mathbf{x}_p^e)]\}G(\mathbf{x}; \mathbf{x}')dV(\mathbf{x}'). \quad (\text{A2})$$

In weak-form methods (such as the finite element method (FEM) or SEM), the traction source term in the weak form becomes

$$\int_V w(\mathbf{x})T(\mathbf{x}_p^e)\delta(\mathbf{x} - \mathbf{x}_p^e)dV(\mathbf{x}) = w(\mathbf{x}_p^e)T(\mathbf{x}_p^e), \quad (\text{A3})$$

where $w(\mathbf{x})$ is the abovementioned test function introduced in the second hybrid simulation. The moment–density tensor source term becomes

$$\int_V w(\mathbf{x})\partial_i[m_i(\mathbf{x}_p^e)\delta(\mathbf{x} - \mathbf{x}_p^e)]dV(\mathbf{x}) = -\partial_i w(\mathbf{x}_p^e)m_i(\mathbf{x}_p^e), \quad (\text{A4})$$

which is similar to the moment tensor implementation in Komatitsch and Tromp (1999).

Appendix B Absorbing Boundary Condition implementation of the VM hybrid method

When the hybrid inputs are imposed on the local target model M_{l1} , the resultant potential q_1 on the hybrid interface S is

$$q_1 = q_0 + q_{\text{scatter}}, \quad (\text{B1})$$

where q_{scatter} is the scattered potential owing to the existence of heterogeneity in the local target model M_{l1} . The ABC (Clayton & Engquist, 1977) can be used to absorb the scattered potential $\nabla q_{\text{scatter}}$ on the hybrid interface S as follows:

$$\mathbf{n} \cdot \nabla q_{\text{scatter}} = -\sqrt{\frac{\rho}{\kappa}} \partial_t q_{\text{scatter}}, \quad (\text{B2})$$

1049 where \mathbf{n} is the unit outward normal of the boundary $\partial\Omega$. With the hybrid inputs ∇q_0
 1050 and $\partial_t q_0$, the second-order explicit Newmark time-marching scheme (Newmark, 1959)
 1051 can be used to perform the hybrid simulation in the local target model M_{l1} in the frame-
 1052 work of SEM:

$$\mathbf{M}_1 \ddot{\mathbf{Q}}_1 + \mathbf{C}_1 (\dot{\mathbf{Q}}_1 - \dot{\mathbf{Q}}_0) + \mathbf{K}_1 \mathbf{Q}_1 = \mathbf{F}_0^T, \quad (\text{B3})$$

1053 where the \mathbf{C}_1 vector is obtained from the ABC, and $\dot{\mathbf{Q}}_1$ and $\dot{\mathbf{Q}}_0$ are the temporal deriva-
 1054 tives of the potential vector calculated in the local target and reference models. \mathbf{M}_1 is
 1055 the global mass matrix, and \mathbf{K}_1 is the global stiffness matrix assigned to the local tar-
 1056 get model M_{l1} . Note that Equation (B2) is used to absorb only the scattered waves and
 1057 not the total wavefield. This boundary treatment naturally combines the forward wave-
 1058 field with DSM or FK solutions and is the key part of the VM hybrid implementation.

1059 Appendix C Best Scenario for the YM Method

1060 In the best scenario, when the hybrid interface S completely follows the boundary
 1061 of elements, namely, a Heaviside window function is adopted such that the diagonal value
 1062 \mathbf{W} of all the points in the local domain Ω_l and on the hybrid interface S (e.g., the closed
 1063 green line in Figure 2) is nonzero. The conceptual illustration of local target model M_{l1}
 1064 associated with the YM method in this best scenario is depicted in Figure 1e, the blue
 1065 part is where the hybrid input is imposed and the green part corresponds to the PML
 1066 domain. Note that the blue part in Figure 1e for imposing the numerical hybrid inputs
 1067 is outside the local target model M_{l1} . Masson et al. (2014) suggests that only part of
 1068 values of the internal forces $\mathbf{W}^e(\mathbf{K}_0^e \cdot \mathbf{Q}_0^e)$ and $\mathbf{W}^e \mathbf{Q}_0^e$ at the GLL nodes exactly on the
 1069 hybrid interface S must be recorded according to the inner scheme in Equation (13) cor-
 1070 responding to the closed green line in the blue elements (hybrid elements in the BY hy-
 1071 brid method) in Figure 2. Because only the hybrid elements contribute to the numer-
 1072 ical hybrid inputs, $\mathbf{W}^e(\mathbf{K}_0^e \cdot \mathbf{Q}_0^e)$ and $\mathbf{W}^e \mathbf{Q}_0^e$ are related to only the GLL points on the
 1073 hybrid interfaces under the selection of the element window function matrix \mathbf{W}^e . Note
 1074 that in the best scenario, as in Figure 1e, although the blue domain is outside the hy-
 1075 brid interface S , it is an inner scheme as defined in Masson et al. (2014).

1076 References

- 1077 Aki, K., & Richards, P. G. (2002). Quantitative seismology, 2nd ed.
 1078 Basabe, J. D. D., & Sen, M. K. (2007). Grid dispersion and stability criteria of
 1079 some common finite-element methods for acoustic and elastic wave equations.
 1080 Geophysics, 72(6), T81-T95. Retrieved from [https://doi.org/10.1190/](https://doi.org/10.1190/1.2785046)
 1081 1.2785046 doi: 10.1190/1.2785046

- 1082 Beller, S., Monteiller, V., Operto, S., Nolet, G., Paul, A., & Zhao, L. (2018). Litho-
1083 spheric architecture of the south-western Alps revealed by multiparameter
1084 teleseismic full-waveform inversion. *Geophysical Journal International*, *212*(2),
1085 1369-1388. Retrieved from <http://dx.doi.org/10.1093/gji/ggx216> doi:
1086 10.1093/gji/ggx216
- 1087 Bielak, J., Loukakis, K., Hisada, Y., & Yoshimura, C. (2003). Domain reduction
1088 method for three-dimensional earthquake modeling in localized regions, part i:
1089 Theory. *Bulletin of the Seismological Society of America*, *93*(2), 817-824.
- 1090 Boehm, C., Hanzich, M., de la Puente, J., & Fichtner, A. (2016). Wavefield compres-
1091 sion for adjoint methods in full-waveform inversion. *Geophysics*, *81*(6), R385-
1092 R397. Retrieved from <https://doi.org/10.1190/geo2015-0653.1> doi: 10
1093 .1190/geo2015-0653.1
- 1094 Bozdog, E., Peter, D., Lefebvre, M., Komatitsch, D., Tromp, J., Hill, J., ... Pug-
1095 mire, D. (2016). Global adjoint tomography: first-generation model.
1096 *Geophysical Journal International*, *207*. Retrieved from [https://doi.org/](https://doi.org/10.1093/gji/ggw356)
1097 [10.1093/gji/ggw356](https://doi.org/10.1093/gji/ggw356) doi: 10.1093/gji/ggw356
- 1098 Capdeville, Y. (2021, 05). Homogenization of seismic point and extended sources.
1099 *Geophysical Journal International*, *226*(2), 1390-1416. Retrieved from
1100 <https://doi.org/10.1093/gji/ggab178> doi: 10.1093/gji/ggab178
- 1101 Capdeville, Y., Chaljub, E., Vilotte, J. P., & Montagner, J. P. (2003). Coupling
1102 the spectral element method with a modal solution for elastic wave propaga-
1103 tion in global earth models. *Geophysical Journal International*, *152*(1), 34-67.
1104 Retrieved from [https://onlinelibrary.wiley.com/doi/abs/10.1046/](https://onlinelibrary.wiley.com/doi/abs/10.1046/j.1365-246X.2003.01808.x)
1105 [j.1365-246X.2003.01808.x](https://onlinelibrary.wiley.com/doi/abs/10.1046/j.1365-246X.2003.01808.x) doi: 10.1046/j.1365-246X.2003.01808.x
- 1106 Capdeville, Y., Guillot, L., & Marigo, J. (2010). 2-D non-periodic homogenization
1107 to upscale elastic media for P-SV waves. *Geophysical Journal International*,
1108 *182*(2), 903-922. Retrieved from [https://onlinelibrary.wiley.com/doi/](https://onlinelibrary.wiley.com/doi/abs/10.1111/j.1365-246X.2010.04636.x)
1109 [abs/10.1111/j.1365-246X.2010.04636.x](https://onlinelibrary.wiley.com/doi/abs/10.1111/j.1365-246X.2010.04636.x) doi: 10.1111/j.1365-246X.2010
1110 .04636.x
- 1111 Capdeville, Y., & Mtivier, L. (2018). Elastic full waveform inversion based on the
1112 homogenization method: theoretical framework and 2-d numerical illustra-
1113 tions. *Geophysical Journal International*, *213*(2), 1093-1112. Retrieved from
1114 <http://dx.doi.org/10.1093/gji/ggy039> doi: 10.1093/gji/ggy039
- 1115 Chen, L., Wen, L., & Zheng, T. (2005). A wave equation migration method for
1116 receiver function imaging: 1. theory. *Journal of Geophysical Research: Solid*
1117 *Earth*, *110*(B11). Retrieved from [https://agupubs.onlinelibrary.wiley](https://agupubs.onlinelibrary.wiley.com/doi/abs/10.1029/2005JB003665)
1118 [.com/doi/abs/10.1029/2005JB003665](https://agupubs.onlinelibrary.wiley.com/doi/abs/10.1029/2005JB003665) doi: 10.1029/2005JB003665

- 1119 Chevrot, S., Favier, N., & Komatitsch, D. (2004). Shear wave splitting in three-
1120 dimensional anisotropic media. *Geophysical Journal International*, *159*(2), 711-
1121 720. Retrieved from <https://doi.org/10.1111/j.1365-246X.2004.02432.x>
1122 doi: 10.1111/j.1365-246X.2004.02432.x
- 1123 Clayton, R., & Engquist, B. (1977). Absorbing boundary conditions for acoustic and
1124 elastic wave equations. *Bulletin of the Seismological Society of America*, *67*(6),
1125 1529-1540.
- 1126 Clouzet, P., Masson, Y., & Romanowicz, B. (2018). Box Tomography: first appli-
1127 cation to the imaging of upper-mantle shear velocity and radial anisotropy
1128 structure beneath the North American continent. *Geophysical Journal*
1129 *International*, *213*(3), 1849-1875. Retrieved from <https://doi.org/10.1093/gji/ggy078>
1130 doi: 10.1093/gji/ggy078
- 1131 Cupillard, P., Delavaud, E., Burgos, G., Festa, G., Vilotte, J.-P., Capdeville,
1132 Y., & Montagner, J.-P. (2012). Regsem: a versatile code based on the
1133 spectral element method to compute seismic wave propagation at the re-
1134 gional scale. *Geophysical Journal International*, *188*(3), 1203-1220. doi:
1135 10.1111/j.1365-246X.2011.05311.x
- 1136 Deville, M. O., Fischer, P. F., & Mund, E. H. (2002). *High-order methods*
1137 *for incompressible fluid flow*. Cambridge University Press. doi: 10.1017/
1138 CBO9780511546792
- 1139 Fichtner, A., Kennett, B. L. N., Igel, H., & Bunge, H. (2009). Full seismic wave-
1140 form tomography for uppermantle structure in the australasian region using
1141 adjoint methods. *Geophysical Journal International*, *179*(3), 1703-1725.
1142 Retrieved from [https://onlinelibrary.wiley.com/doi/abs/10.1111/
1143 j.1365-246X.2009.04368.x](https://onlinelibrary.wiley.com/doi/abs/10.1111/j.1365-246X.2009.04368.x) doi: 10.1111/j.1365-246X.2009.04368.x
- 1144 Fichtner, A., vanHerwaarden, D.-P., Afanasiev, M., Simut, S., Krischer, L., ubuk-
1145 Sabuncu, Y., ... Igel, H. (2018). The collaborative seismic earth model:
1146 Generation 1. *Geophysical Research Letters*, *45*(9), 4007-4016. Retrieved
1147 from [https://agupubs.onlinelibrary.wiley.com/doi/abs/10.1029/
1148 2018GL077338](https://agupubs.onlinelibrary.wiley.com/doi/abs/10.1029/2018GL077338) doi: 10.1029/2018gl077338
- 1149 French, S. W., & Romanowicz, B. (2015). Broad plumes rooted at the base of the
1150 earth's mantle beneath major hotspots. *Nature*, *525*(7567), 95-99. Retrieved
1151 from <https://doi.org/10.1038/nature14876> doi: 10.1038/nature14876
- 1152 French, S. W., & Romanowicz, B. A. (2014). Whole-mantle radially anisotropic
1153 shear velocity structure from spectral-element waveform tomography.
1154 *Geophysical Journal International*, *199*(3), 1303-1327. Retrieved from
1155 <https://doi.org/10.1093/gji/ggu334> doi: 10.1093/gji/ggu334

- 1156 Godinho, L., Amado Mendes, P., Tadeu, A., Cadena-Isaza, A., Smerzini, C., Snchez-
1157 Sesma, F. J., ... Komatitsch, D. (2009). Numerical Simulation of Ground
1158 Rotations along 2D Topographical Profiles under the Incidence of Elastic
1159 Plane Waves. Bulletin of the Seismological Society of America, 99(2B),
1160 1147-1161. Retrieved from <https://doi.org/10.1785/0120080096> doi:
1161 10.1785/0120080096
- 1162 Kawai, K., Takeuchi, N., & Geller, R. J. (2006). Complete synthetic seismo-
1163 grams up to 2 Hz for transversely isotropic spherically symmetric media.
1164 Geophysical Journal International, 164(2), 411-424. Retrieved from [https://](https://onlinelibrary.wiley.com/doi/abs/10.1111/j.1365-246X.2005.02829.x)
1165 onlinelibrary.wiley.com/doi/abs/10.1111/j.1365-246X.2005.02829.x
1166 doi: 10.1111/j.1365-246X.2005.02829.x
- 1167 Kennett, B. L. N., Engdahl, E. R., & Buland, R. (1995). Constraints on
1168 seismic velocities in the Earth from traveltimes. Geophysical Journal
1169 International, 122(1), 108-124. Retrieved from [https://doi.org/10.1111/](https://doi.org/10.1111/j.1365-246X.1995.tb03540.x)
1170 [j.1365-246X.1995.tb03540.x](https://doi.org/10.1111/j.1365-246X.1995.tb03540.x) doi: 10.1111/j.1365-246X.1995.tb03540.x
- 1171 Koene, E. F. M., Robertsson, J. O. A., Brogini, F., & Andersson, F. (2018). Elim-
1172 inating time dispersion from seismic wave modeling. Geophysical Journal
1173 International, 213(1), 169-180. Retrieved from [http://dx.doi.org/10.1093/](http://dx.doi.org/10.1093/gji/ggx563)
1174 [gji/ggx563](http://dx.doi.org/10.1093/gji/ggx563) doi: 10.1093/gji/ggx563
- 1175 Komatitsch, D., Ritsema, J., & Tromp, J. (2002). The spectral-element method, be-
1176 lowulf computing, and global seismology. SCIENCE, 298(5599), 1737-1742. doi:
1177 10.1126/science.1076024
- 1178 Komatitsch, D., & Tromp, J. (1999). Introduction to the spectral element
1179 method for three-dimensional seismic wave propagation. Geophysical Journal
1180 International, 139(3), 806-822. Retrieved from [https://onlinelibrary](https://onlinelibrary.wiley.com/doi/abs/10.1046/j.1365-246x.1999.00967.x)
1181 [.wiley.com/doi/abs/10.1046/j.1365-246x.1999.00967.x](https://onlinelibrary.wiley.com/doi/abs/10.1046/j.1365-246x.1999.00967.x) doi: 10.1046/
1182 [j.1365-246x.1999.00967.x](https://onlinelibrary.wiley.com/doi/abs/10.1046/j.1365-246x.1999.00967.x)
- 1183 Komatitsch, D., Xie, Z., Bozdağ, E., Sales de Andrade, E., Peter, D., Liu, Q., &
1184 Tromp, J. (2016). Anelastic sensitivity kernels with parsimonious storage
1185 for adjoint tomography and full waveform inversion. Geophysical Journal
1186 International, 206(3), 1467-1478. doi: 10.1093/gji/ggw224
- 1187 Lei, W., Ruan, Y., Bozda, E., Peter, D., Lefebvre, M., Komatitsch, D., ... Pugmire,
1188 D. (2020). Global adjoint tomography-model GLAD-M25. Geophysical Journal
1189 International, 223(1), 1-21. Retrieved from [https://doi.org/10.1093/gji/](https://doi.org/10.1093/gji/ggaa253)
1190 [ggaa253](https://doi.org/10.1093/gji/ggaa253) doi: 10.1093/gji/ggaa253
- 1191 Leng, K., Hosseini, K., Nissen-Meyer, T., van Driel, M., & Al-Attar, D. (2019).
1192 Axisem3D: broadband seismic wavefields in 3-D global earth models with un-

- 1193 dulating discontinuities. Geophysical Journal International. Retrieved from
1194 <https://dx.doi.org/10.1093/gji/ggz092> doi: 10.1093/gji/ggz092
- 1195 Leng, K., Korenaga, J., & Nissen-Meyer, T. (2020). 3-D scattering of elastic waves
1196 by small-scale heterogeneities in the Earth's mantle. Geophysical Journal
1197 International, *223*(1), 502-525. Retrieved from <https://doi.org/10.1093/gji/ggaa331>
1198 doi: 10.1093/gji/ggaa331
- 1199 Lin, C., Monteiller, V., Wang, K., Liu, T., Tong, P., & Liu, Q. (2019). High-
1200 frequency seismic wave modelling of the deep earth based on hybrid methods
1201 and spectral-element simulations: a conceptual study. Geophysical Journal
1202 International, *219*(3), 1948-1969. Retrieved from <https://doi.org/10.1093/gji/ggz413>
1203 doi: 10.1093/gji/ggz413
- 1204 Lyu, C., Capdeville, Y., Al-Attar, D., & Zhao, L. (2021). Intrinsic non-uniqueness of
1205 the acoustic full waveform inverse problem. Geophysical Journal International.
1206 Retrieved from <https://doi.org/10.1093/gji/ggab134> doi: 10.1093/gji/
1207 ggab134
- 1208 Lyu, C., Capdeville, Y., Lu, G., & Zhao, L. (2021). Removing the Courant-
1209 Friedrichs-Lewy stability criterion of the explicit time-domain very high degree
1210 spectral-element method with eigenvalue perturbation. Geophysics, *86*(5),
1211 T411-T419. Retrieved from <https://doi.org/10.1190/geo2020-0623.1> doi:
1212 10.1190/geo2020-0623.1
- 1213 Lyu, C., Capdeville, Y., & Zhao, L. (2020). Efficiency of the spectral element
1214 method with very high polynomial degree to solve the elastic wave equation.
1215 Geophysics, *85*(1), T33-T43. Retrieved from <https://doi.org/10.1190/geo2019-0087.1>
1216 doi: 10.1190/geo2019-0087.1
- 1217 Masson, Y., Cupillard, P., Capdeville, Y., & Romanowicz, B. (2014). On
1218 the numerical implementation of time-reversal mirrors for tomographic
1219 imaging. Geophysical Journal International, *196*(3), 1580-1599. Re-
1220 trieved from <https://hal.archives-ouvertes.fr/hal-01303023> doi:
1221 10.1093/gji/ggt459
- 1222 Masson, Y., & Romanowicz, B. (2017a). Box tomography: localized imaging of re-
1223 mote targets buried in an unknown medium, a step forward for understanding
1224 key structures in the deep earth. Geophysical Journal International, *211*(1),
1225 141-163. Retrieved from <https://dx.doi.org/10.1093/gji/ggx141> doi:
1226 10.1093/gji/ggx141
- 1227 Masson, Y., & Romanowicz, B. (2017b). Fast computation of synthetic seismograms
1228 within a medium containing remote localized perturbations: a numerical so-
1229 lution to the scattering problem. Geophysical Journal International, *208*(2),

- 1230 674-692. Retrieved from <http://dx.doi.org/10.1093/gji/ggw412> doi:
1231 10.1093/gji/ggw412
- 1232 Monteiller, V., Beller, S., Plazolles, B., & Chevrot, S. (2020). On the validity of
1233 the planar wave approximation to compute synthetic seismograms of teleseis-
1234 mic body waves in a 3-D regional model. *Geophysical Journal International*,
1235 224(3), 2060-2076. Retrieved from <https://doi.org/10.1093/gji/ggaa570>
1236 doi: 10.1093/gji/ggaa570
- 1237 Monteiller, V., Chevrot, S., Komatitsch, D., & Fuji, N. (2013). A hybrid method
1238 to compute short-period synthetic seismograms of teleseismic body waves
1239 in a 3-D regional model. *Geophysical Journal International*, 192(1), 230-
1240 247. Retrieved from <https://doi.org/10.1093/gji/ggs006> doi:
1241 10.1093/gji/ggs006
- 1242 Monteiller, V., Chevrot, S., Komatitsch, D., & Wang, Y. (2015). Three-dimensional
1243 full waveform inversion of short-period teleseismic wavefields based upon the
1244 semdsm hybrid method. *Geophysical Journal International*, 202(2), 811-
1245 827. Retrieved from [http://gji.oxfordjournals.org/content/202/2/
1246 811.abstract](http://gji.oxfordjournals.org/content/202/2/811.abstract) doi: 10.1093/gji/ggv189
- 1247 Newmark, N. M. (1959). A method of computation for structural dynamics..
- 1248 Nissen-Meyer, T., Fournier, A., & Dahlen, F. A. (2007). A twodimensional spec-
1249 tralelement method for computing sphericalearth seismograms i. moment-
1250 tensor source. *Geophysical Journal International*, 168(3), 1067-1092. Re-
1251 trieved from <http://dx.doi.org/10.1111/j.1365-246X.2006.03121.x> doi:
1252 10.1111/j.1365-246X.2006.03121.x
- 1253 Nissen-Meyer, T., van Driel, M., Sthler, S. C., Hosseini, K., Hempel, S., Auer,
1254 L., ... Fournier, A. (2014). Axisem: broadband 3-D seismic wave-
1255 fields in axisymmetric media. *Solid Earth*, 5(1), 425-445. Retrieved from
1256 <http://www.solid-earth.net/5/425/2014/> doi: 10.5194/se-5-425-2014
- 1257 Pienkowska, M., Monteiller, V., & Nissen-Meyer, T. (2021). High-frequency global
1258 wavefields for local 3-D structures by wavefield injection and extrapolation.
1259 *Geophysical Journal International*, 225(3), 1782–1798.
- 1260 Pratt, R. G., Shin, C., & Hick, G. (1998). Gaussnewton and full newton methods in
1261 frequencyspace seismic waveform inversion. *Geophysical Journal International*,
1262 133(2), 341-362.
- 1263 Robertsson, J. O. A., & Chapman, C. H. (2000). An efficient method for calculating
1264 finitedifference seismograms after model alterations. *Geophysics*, 65(3), 907-
1265 918. Retrieved from <http://library.seg.org/doi/abs/10.1190/1.1444787>
1266 doi: 10.1190/1.1444787

- 1267 Seriani, G., & Oliveira, S. (2008). Dispersion analysis of spectral element methods
 1268 for elastic wave propagation. *Wave Motion*, 45(6), 729 - 744. Retrieved from
 1269 <http://www.sciencedirect.com/science/article/pii/S0165212507001163>
 1270 doi: <https://doi.org/10.1016/j.wavemoti.2007.11.007>
- 1271 Tarantola, A. (1984). Inversion of seismic reflection data in the acoustic approxi-
 1272 mation. *Geophysics*, 49(8), 1259-1266. Retrieved from [https://doi.org/10](https://doi.org/10.1190/1.1441754)
 1273 [.1190/1.1441754](https://doi.org/10.1190/1.1441754) doi: 10.1190/1.1441754
- 1274 Tong, P., Chen, C., Komatitsch, D., Basini, P., & Liu, Q. (2014). High-resolution
 1275 seismic array imaging based on an SEM-FK hybrid method. *Geophysical*
 1276 *Journal International*, 197(1), 369-395. Retrieved from [http://dx.doi.org/](http://dx.doi.org/10.1093/gji/ggt508)
 1277 [10.1093/gji/ggt508](http://dx.doi.org/10.1093/gji/ggt508) doi: 10.1093/gji/ggt508
- 1278 Tong, P., Komatitsch, D., Tseng, T., Hung, S., Chen, C., Basini, P., & Liu, Q.
 1279 (2014). A 3-D spectral-element and frequency-wave number hybrid method for
 1280 high-resolution seismic array imaging. *Geophysical Research Letters*, 41(20),
 1281 7025-7034.
- 1282 Tromp, J. (2019). Seismic wavefield imaging of earths interior across scales. *Nature*
 1283 *Reviews Earth & Environment*. Retrieved from [https://doi.org/10.1038/](https://doi.org/10.1038/s43017-019-0003-8)
 1284 [s43017-019-0003-8](https://doi.org/10.1038/s43017-019-0003-8) doi: 10.1038/s43017-019-0003-8
- 1285 Virieux, J., & Operto, S. (2009). An overview of full-waveform inversion in ex-
 1286 ploration geophysics. *Geophysics*, 74(6), WCC1-WCC26. Retrieved from
 1287 <https://doi.org/10.1190/1.3238367> doi: 10.1190/1.3238367
- 1288 Wang, K., Wang, Y., Song, X., Tong, P., Liu, Q., & Yang, Y. (2021, 08). Full-
 1289 Waveform Inversion of HighFrequency Teleseismic Body Waves Based on
 1290 Multiple PlaneWave Incidence: Methods and Practical Applications. *Bulletin*
 1291 *of the Seismological Society of America*, 112(1), 118-132. Retrieved from
 1292 <https://doi.org/10.1785/0120210094> doi: 10.1785/0120210094
- 1293 Wang, K., Yang, Y., Jiang, C., Wang, Y., Tong, P., Liu, T., & Liu, Q. (2021). Ad-
 1294 joint tomography of ambient noise data and teleseismic p waves: Method-
 1295 ology and applications to central california. *Journal of Geophysical*
 1296 *Research: Solid Earth*, 126(6), e2021JB021648. Retrieved from [https://](https://agupubs.onlinelibrary.wiley.com/doi/abs/10.1029/2021JB021648)
 1297 agupubs.onlinelibrary.wiley.com/doi/abs/10.1029/2021JB021648
 1298 (e2021JB021648 2021JB021648) doi: <https://doi.org/10.1029/2021JB021648>
- 1299 Wang, Y., Chevrot, S., Monteiller, V., Komatitsch, D., Mouthereau, F., Manatschal,
 1300 G., ... Martin, R. (2016). The deep roots of the western Pyrenees revealed
 1301 by full waveform inversion of teleseismic p waves. *Geology*, 44(6), 475-U100.
 1302 Retrieved from <GotoISI>://WOS:000378203600021 doi: 10.1130/g37812.1
- 1303 Wen, L., & Helmberger, D. V. (1998). A two-dimensional P-SV hybrid method and

- 1304 its application to modeling localized structures near the core-mantle boundary.
1305 Journal of Geophysical Research: Solid Earth, 103(B8), 17901-17918.
- 1306 Xie, Z., Komatitsch, D., Martin, R., & Matzen, R. (2014). Improved forward wave
1307 propagation and adjoint-based sensitivity kernel calculations using a numer-
1308 ically stable finite-element PML. Geophysical Journal International, 198(3),
1309 1714-1747. Retrieved from <https://doi.org/10.1093/gji/ggu219> doi:
1310 10.1093/gji/ggu219
- 1311 Yoshimura, C., Bielak, J., Hisada, Y., & Fernández, A. (2003). Domain reduc-
1312 tion method for three-dimensional earthquake modeling in localized regions,
1313 Part II: verification and applications. Bulletin of the Seismological Society
1314 of America, 93(2), 825-841. Retrieved from [https://doi.org/10.1785/](https://doi.org/10.1785/0120010252)
1315 [0120010252](https://doi.org/10.1785/0120010252) doi: 10.1785/0120010252
- 1316 Zhang, C., Yao, H., Liu, Q., Zhang, P., Yuan, Y. O., Feng, J., & Fang, L. (2018).
1317 Linear array ambient noise adjoint tomography reveals intense crust-mantle
1318 interactions in north china craton. Journal of Geophysical Research: Solid
1319 Earth, 123(1), 368-383. Retrieved from [https://agupubs.onlinelibrary](https://agupubs.onlinelibrary.wiley.com/doi/abs/10.1002/2017JB015019)
1320 [.wiley.com/doi/abs/10.1002/2017JB015019](https://doi.org/10.1002/2017JB015019) doi: [https://doi.org/10.1002/](https://doi.org/10.1002/2017JB015019)
1321 [2017JB015019](https://doi.org/10.1002/2017JB015019)
- 1322 Zhao, L., Paul, A., Guillot, S., Solarino, S., Malus, M. G., Zheng, T., ... Schwartz,
1323 S. (2015). First seismic evidence for continental subduction beneath the
1324 western alps. Geology, 43(9), 815-818.
- 1325 Zhao, L., Wen, L., Chen, L., & Zheng, T. (2008). A two-dimensional hybrid
1326 method for modeling seismic wave propagation in anisotropic media. Journal
1327 of Geophysical Research: Solid Earth, 113(B12), n/a-n/a. Retrieved from
1328 <http://dx.doi.org/10.1029/2008JB005733> doi: 10.1029/2008JB005733
- 1329 Zhao, L., Zhao, M., & Lu, G. (2014). Upper mantle seismic anisotropy beneath a
1330 convergent boundary: SKS waveform modeling in central tibet. Science China:
1331 Earth Sciences, 57, 759-776. Retrieved from [https://doi.org/10.1007/](https://doi.org/10.1007/s11430-014-4826-3)
1332 [s11430-014-4826-3](https://doi.org/10.1007/s11430-014-4826-3) doi: 10.1007/s11430-014-4826-3
- 1333 Zhao, M., Capdeville, Y., & Zhang, H. (2016). Direct numerical modeling of
1334 time-reversal acoustic subwavelength focusing. Wave Motion, 67, 102-115.
1335 Retrieved from [http://www.sciencedirect.com/science/article/pii/](http://www.sciencedirect.com/science/article/pii/S0165212516300877)
1336 [S0165212516300877](https://doi.org/10.1016/j.wavemoti.2016.07.010) doi: <https://doi.org/10.1016/j.wavemoti.2016.07.010>
- 1337 Zhu, L., & Rivera, L. A. (2002). A note on the dynamic and static displace-
1338 ments from a point source in multilayered media. Geophysical Journal
1339 International, 148(3), 619-627. Retrieved from [https://doi.org/10.1046/](https://doi.org/10.1046/j.1365-246X.2002.01610.x)
1340 [j.1365-246X.2002.01610.x](https://doi.org/10.1046/j.1365-246X.2002.01610.x) doi: 10.1046/j.1365-246X.2002.01610.x

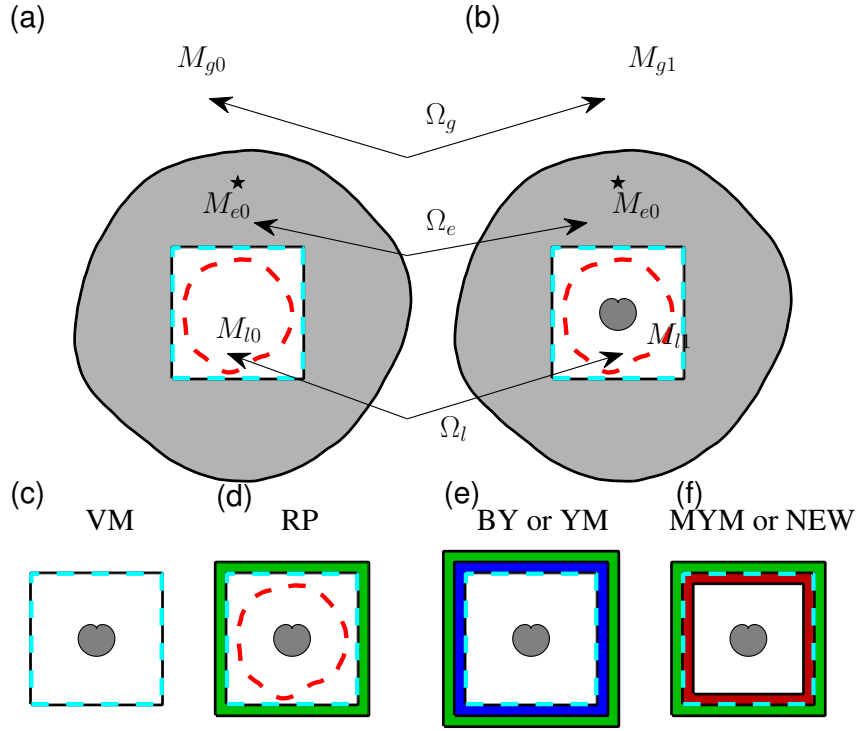


Figure 1. Nomenclatures of the hybrid simulation. (a) The global reference model M_{g0} contains the gray external model M_e and the white local reference model M_{l0} , which are assigned to the global domain Ω_g , external domain Ω_e , and local domain Ω_l , respectively. The red and cyan dashed lines represent hybrid interfaces S . (b) The global target model M_{g1} contains the gray external model M_e and the white local target model M_{l1} , which are also assigned to Ω_g , Ω_e , and Ω_l . The gray cartesian circle represents local target heterogeneity. (c) Local target model M_{l1} and its hybrid interface S (cyan dashed line) of the VM hybrid method. (d) Local target model M_{l1} and its hybrid interfaces S (red and cyan dashed lines) of the RP hybrid method, and the green part represents the PML domain. (e, f) The local target model M_{l1} of the BY, YM, MYM, and new hybrid methods with the green PML part the hybrid elements in SEM (blue part for BY and YM methods, red part for MYM and new methods), and their hybrid interfaces S (cyan dashed lines).

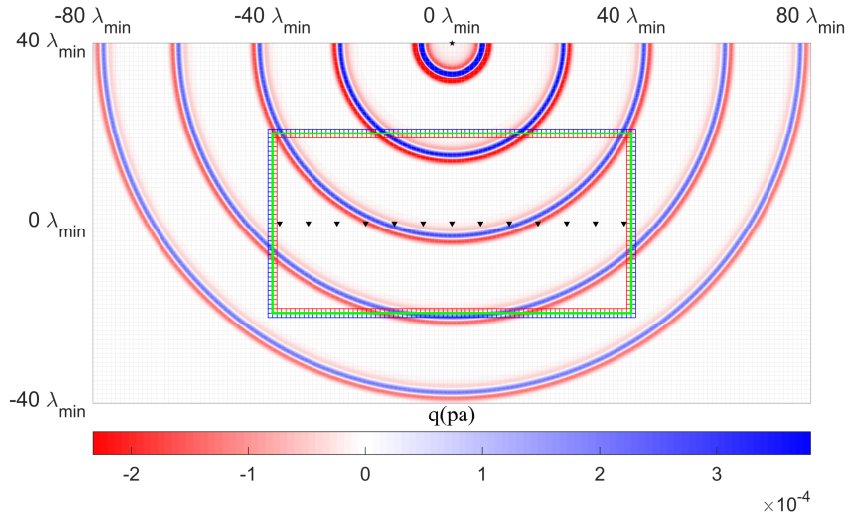


Figure 2. 2D global homogeneous domain Ω_g and wavefields of the potential in the unit of Pascal (pa). The source and 13 receivers are plotted as black star and inverse triangles, respectively. The 160×80 element meshing associated with $N_{GLL} = 8$ are depicted. The wavefields at $13.2 t_{\min}$, $31.2 t_{\min}$, $49.2 t_{\min}$, $67.2 t_{\min}$, and $84 t_{\min}$ are superposed. The green line is the hybrid interface ∂S , the blue elements are the elements used to implement the hybrid injection in Masson et al. (2014), and the red elements are the hybrid elements used in this study.

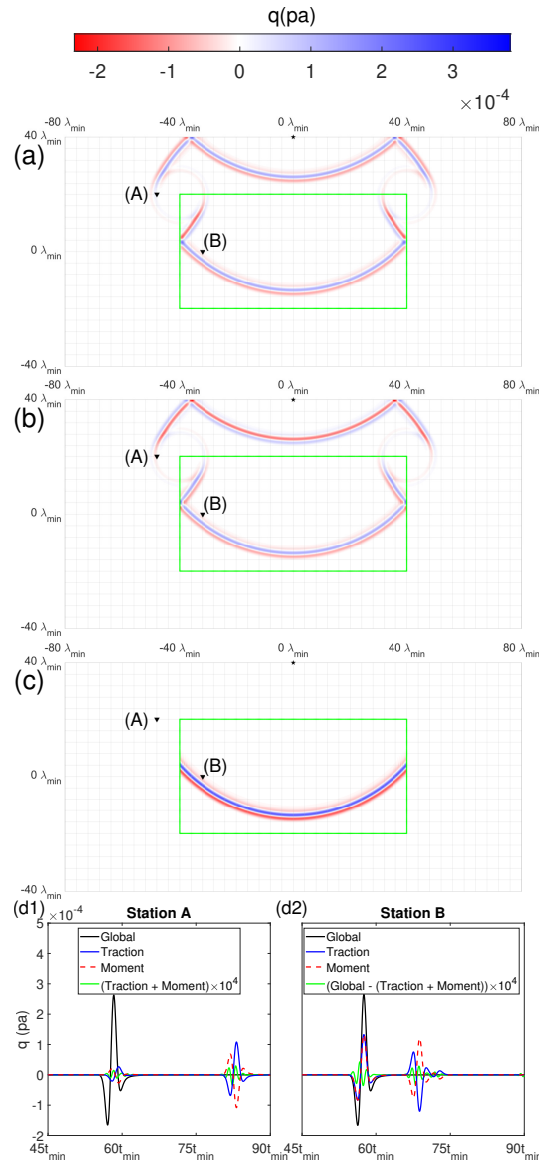


Figure 3. Different contributions of the two surface integrals using the physical representation theorem to perform the hybrid simulation (RP hybrid method). (a) Potential wavefield at $60 t_{\min}$ generated by imposing only the traction surface integral onto the hybrid interface S (green line). (b) Potential wavefield at $60 t_{\min}$ generated by imposing only the moment surface integral onto the hybrid interface. (c) Sum of the wavefields in (a) and (b). (d) Benchmark of waveforms of stations A (d1) and B (d2) as marked in (c). The black, blue, and dashed red waveforms are calculated using the global simulation, hybrid numerical simulation only with the traction surface integral, and hybrid numerical simulation only with the moment surface integral, respectively. The green waveform in (d1) is the enlarged sum of the blue and red dashed waveforms, and the green waveform in (d2) is the enlarged difference between the black waveform and the sum of the blue and red dashed waveforms.

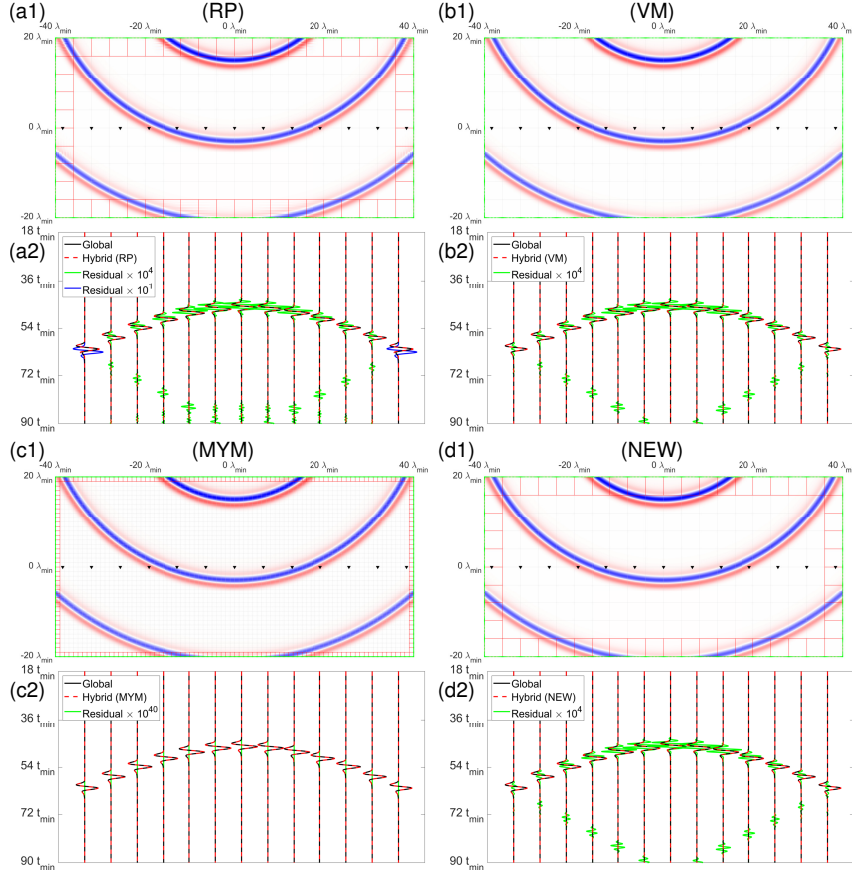


Figure 4. 2D local homogeneous domain Ω_l , hybrid local wavefields (same colorbar as in Figure 2) and waveforms calculated using the four methods. (a1, b1, c1, d1): Superposed wavefields at the same time steps as in Figure 2. The green line is the hybrid interface S , and the red elements are the elements used to implement the associated hybrid method. (a2, b2, c2, d2): Global (solid black lines), hybrid (dotted red lines), and enlarged residual (solid green lines) waveforms. (a1, a2) is from the RP method. (b1, b2) is from the VM method. (c1, c2) is obtained from the MYM method. (d1, d2) is from the new method.

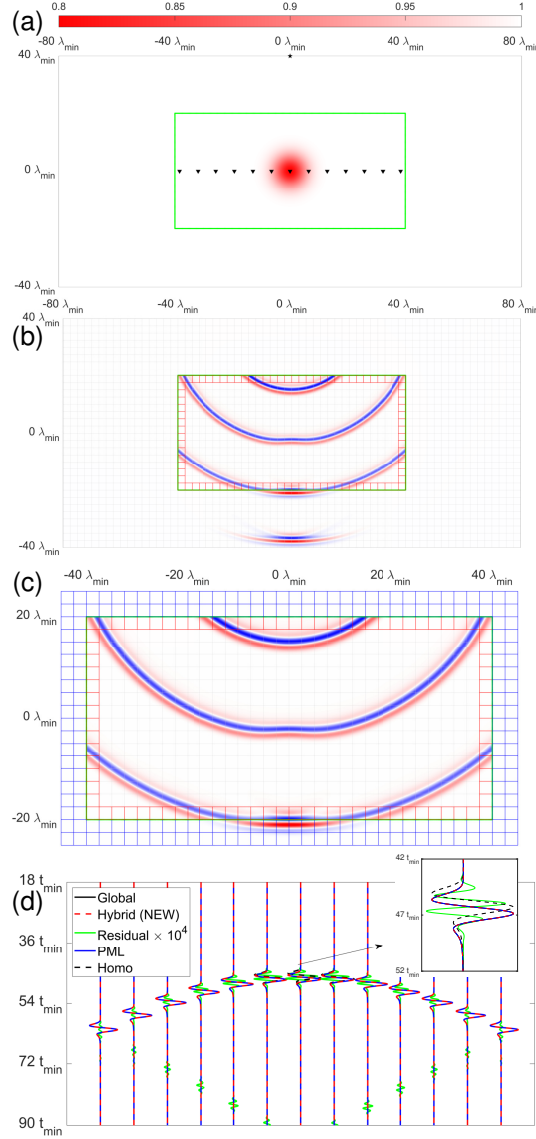


Figure 5. Hybrid simulation in the 2D Gaussian heterogeneous global model using the proposed method. (a) 2D global Gaussian model and hybrid interface S (green line). (b) and (c): Two different hybrid simulations and the associated superposed wavefields (same colorbar as in Figure 2) at the same time steps as in Figure 2, respectively, in the global domain Ω_g and in the local target domain Ω_l with PML absorbing condition. (d) Comparison of different waveforms. The solid black lines represent the global waveforms calculated in the global target model (a). The dotted red lines are the first hybrid waveforms obtained in the global target model, but by imposing the hybrid inputs as shown in (b). The enlarged residuals between the global and first hybrid waveforms are depicted by the solid green lines. The second hybrid waveforms obtained in the local target model (c) with PML in the shrunk domain are depicted as solid blue lines, and the waveforms computed in the 2D homogeneous model are plotted as dotted black lines. Zoomed-in waveforms of the middle station are placed in the upper-right corner of (d).

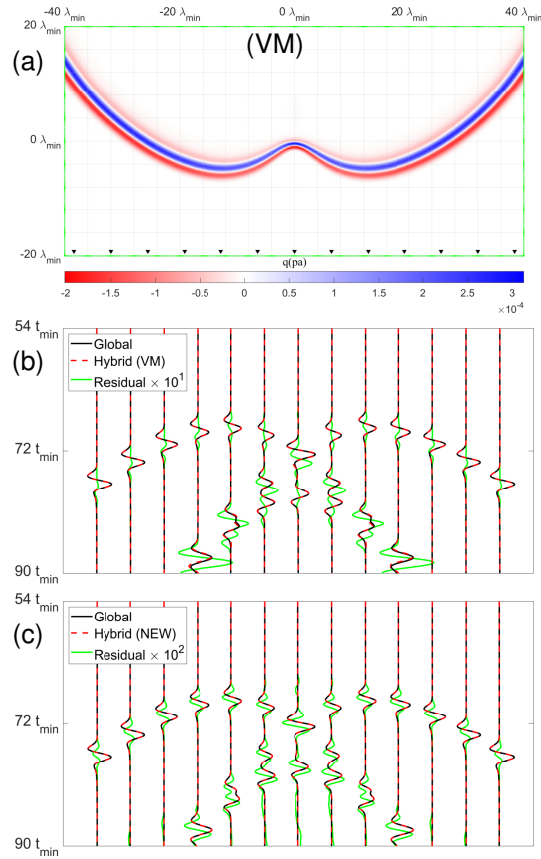


Figure 6. Hybrid simulation in a strong 2D Gaussian heterogeneous model using the VM and new hybrid methods. (a) 2D hybrid wavefield at time step $54 t_{\min}$ by the VM hybrid method. (b, c) Waveform benchmark of VM and new hybrid methods. The solid black lines are the global waveforms calculated in the strong global target model, the dotted red lines are the hybrid waveforms using the VM and new hybrid method, and the dashed green lines are their enlarged residuals; the magnification is 10 for the VM hybrid and 100 for the new hybrid method.

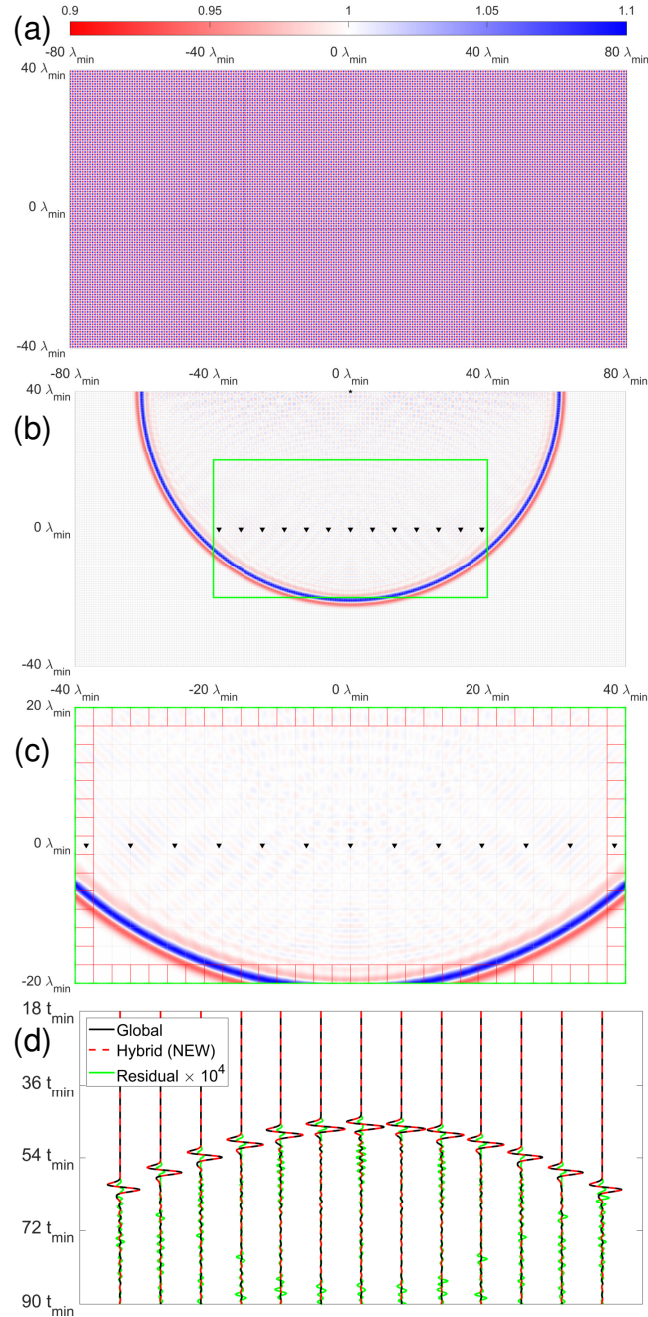


Figure 7. Hybrid simulation in the 2D cosine heterogeneous reference model using the proposed method. (a) 2D cosine heterogeneous model. (b) Global wavefield at $67.2 t_{\min}$ and the 240×120 element meshing associated with $N_{GLL} = 8$ are depicted. (c) Local wavefield at the same time step and the 30×15 element meshing associated with $N_{GLL} = 20$ are depicted. (d) Comparison of the reference waveforms in the solid black lines, hybrid waveforms in the dotted red lines, and enlarged residuals in the solid green lines.

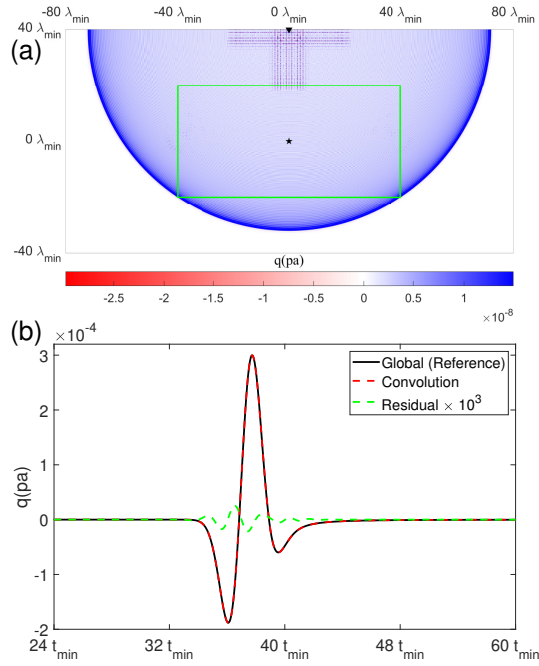


Figure 8. Hybrid simulation in a local reference model using the representation theorem with the source inside and receiver outside. (a) 2D hybrid wavefield related to the calculation of Green's function at time step $72 t_{\min}$. The reverse black triangle is the receiver located outside the box surrounded by the green line, and the black star is the source inside the box. (b) Waveform benchmark. The solid black line is the waveform calculated in the global reference model in Figure 2, the dotted red line is the waveform obtained by the convolution based on the explicit representation theorem, and the dashed green line is the enlarged residual.

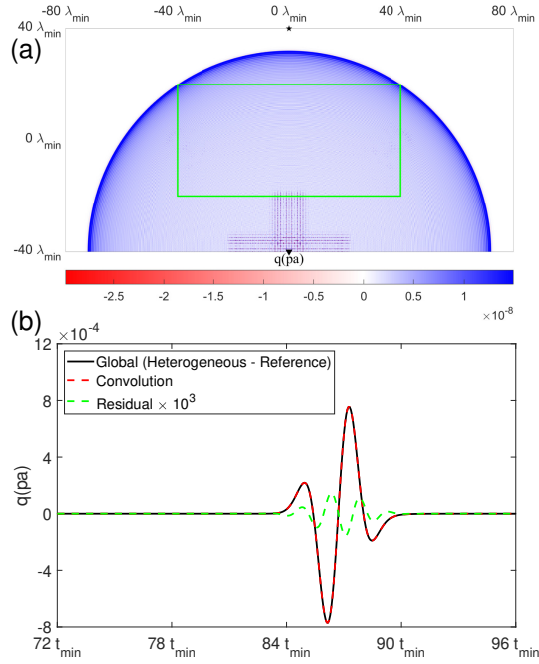


Figure 9. Hybrid simulation in a weak 2D Gaussian heterogeneous model using the new method with the source and the receiver both outside the box. (a) 2D hybrid wavefield at the time step $72 t_{\min}$. (b) Waveform benchmark. The solid black line is the waveform difference between the global waveforms calculated in the global weak Gaussian model in Figure 5 and the global reference model in Figure 2, the dotted red line is the hybrid waveform calculated using the convolution based on the explicit representation theorem, and the dashed green line is the enlarged residual.

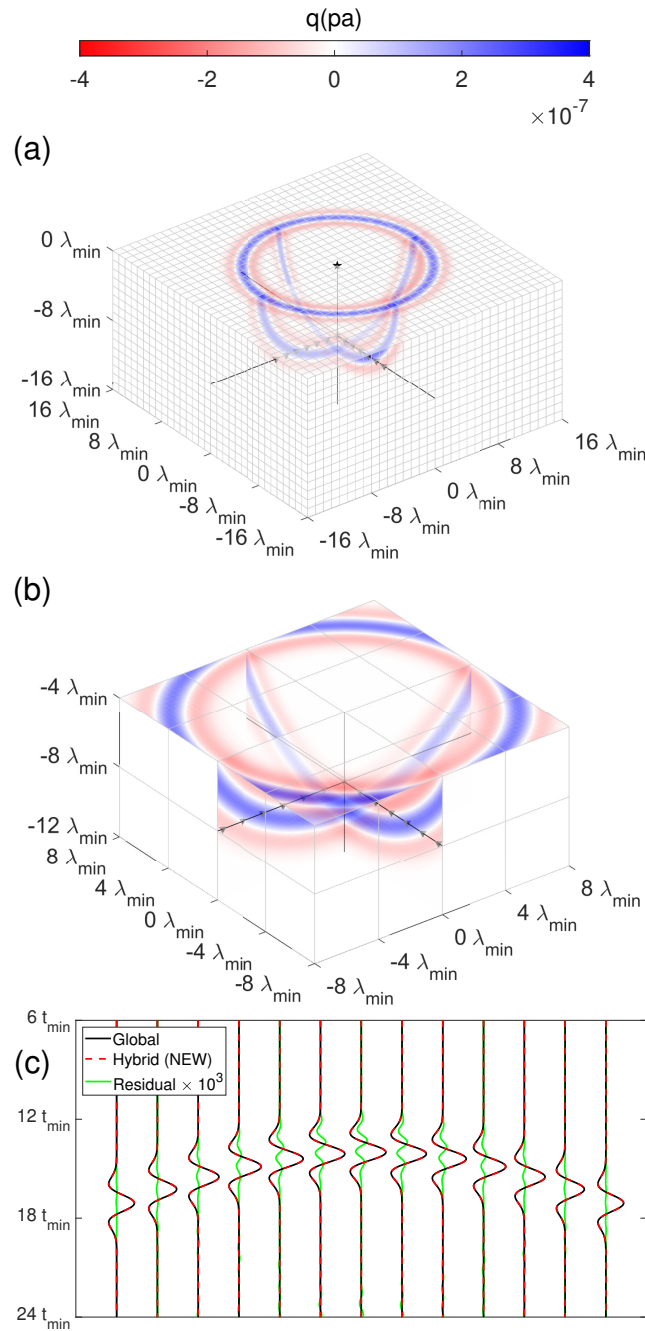


Figure 10. Hybrid simulation in the 3D homogeneous reference model using the proposed method. (a) 3D potential wavefield of global simulation at time step $15.6 t_{\min}$ in the global reference model. (b) Hybrid numerical simulation in the local model. (c) Comparison of the reference waveforms in the solid black lines, hybrid waveforms in the dotted red lines, and enlarged residuals in the solid green lines.

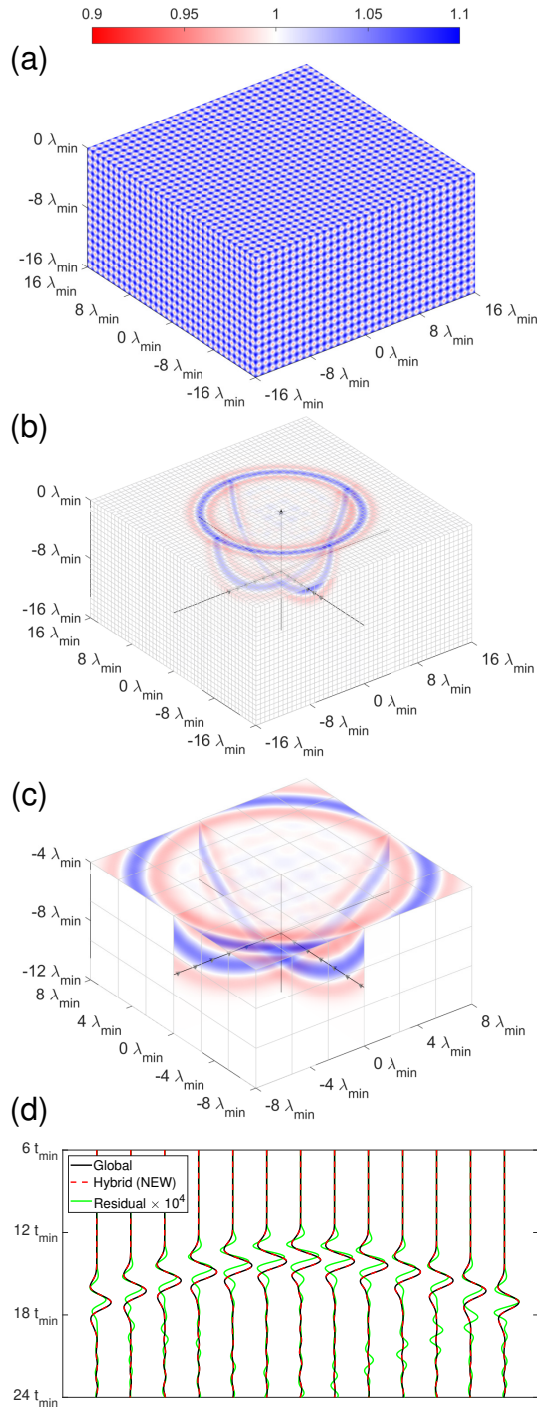


Figure 11. Hybrid simulation in the 3D cosine heterogeneous reference model using the proposed method. (a) 3D cosine heterogeneous model. (b) Potential wavefield of global simulation at time step $15.6 t_{\min}$ in the global model (with the same colorbar as in Figure 10a). (c) Hybrid simulation in the local model at the same time step. (d) Comparison of the reference waveforms in the solid black lines, hybrid waveforms in the dotted red lines, and enlarged residuals in the solid green lines.